



Geology, mineralogy, and cassiterite geochronology of the Ayawilca Zn-Pb-Ag-In-Sn-Cu deposit, Pasco, Peru

Diego Benites¹ · Lisard Torró¹ · Jean Vallance¹ · Oscar Laurent^{2,3} · Patrick Quispe¹ · Silvia Rosas¹ · María Francisca Uzieda⁴ · Christopher S. Holm-Denoma⁵ · Laura S. Pianowski⁵ · Antoni Camprubi⁶ · Vanessa Colás⁶ · Álvaro Fernández-Baca⁷ · Luis Giraldo⁷ · Cyril Chelle-Michou² · Jorge Sáez¹ · Kalin Kouzmanov⁴ · Lluís Fontboté⁴

Received: 5 February 2021 / Accepted: 22 June 2021 / Published online: 13 September 2021
© The Author(s), under exclusive licence to Springer-Verlag GmbH Germany, part of Springer Nature 2021

Abstract

The Ayawilca deposit in Pasco, Peru, represents the most significant recent base-metal discovery in the central Andes and one of the largest undeveloped In resources globally. As of 2018, it hosts an 11.7 Mt indicated resource grading 6.9% Zn, 0.16% Pb, 15 g/t Ag, and 84 g/t In, an additional 45.0 Mt inferred resource grading 5.6% Zn, 0.23% Pb, 17 g/t Ag, and 67 g/t In, and a separate Sn-Cu-Ag inferred resource of 14.5 Mt grading 0.63% Sn, 0.21% Cu, and 18 g/t Ag. Newly obtained U–Pb dates for cassiterite by LA-ICP-MS (22.77 ± 0.41 and 23.05 ± 2.06 Ma) assign the Ayawilca deposit to the Miocene polymetallic belt of central Peru. The polymetallic mineralization occurs as up to 70-m-thick mantos hosted by carbonate rocks of the Late Triassic to Early Jurassic Pucará Group, and subordinately, as steeply dipping veins hosted by rocks of the Pucará Group and overlying Cretaceous sandstones-siltstones of the Goyllarisquizga Group. Relicts of a distal retrograde magnesian skarn and cassiterite (stage pre-A) were identified in the deepest mantos. The volumetrically most important mineralization at Ayawilca comprises a low-sulfidation assemblage (stage A) with quartz, pyrrhotite, arsenopyrite, chalcopyrite, Fe-rich sphalerite, and traces of stannite and herzenbergite. Stage A sphalerite records progressive Fe depletion, from 33 to 10 mol% FeS, which is compatible with the observed transition from low- to a subsequent intermediate-sulfidation stage (B) marked by the crystallization of abundant pyrite and marcasite. Finally, during a later intermediate-sulfidation stage (C) sphalerite (up to 11 mol% FeS), galena, native bismuth, Cu-Pb-Ag sulfosalts, siderite, Mn-Fe carbonates, kaolinite, dickite, and sericite were deposited. This paragenetic evolution shows striking similarities with that at the Cerro de Pasco Cordilleran-type polymetallic deposit, even if at Ayawilca stage C did not reach high-sulfidation conditions. The occurrence of an early retrograde skarn assemblage suggests that the manto bodies at Ayawilca formed at the transition between distal skarn and skarn-free (Cordilleran-type) carbonate-replacement mineralization. Mineral assemblages define a T– fS_2 evolutionary path close to the pyrrhotite-pyrite boundary. Buffering of hydrothermal fluids by underlying Devonian carbonaceous phyllites of the Excelsior Group imposed highly reduced conditions during stage A mineralization ($\log fO_2 < -30$ atm). The low fO_2 favored efficient Sn mobility during stages pre-A and A, in contrast to other known ore deposits in the polymetallic belt of central Peru, in which the occurrence of Sn minerals is minor. Subsequent cooling, progressive sealing of vein walls, and decreasing buffering potential of the host rocks promoted the shift from low- (stage A) to intermediate-sulfidation (stages B and C) states. LA-ICP-MS analyses reveal significant In contents in Fe-rich sphalerite (up to 1.7 wt%), stannite (up to 1908 ppm), and chalcopyrite (up to 1185 ppm). The highest In content was found in stage A sphalerite that precipitated along with chalcopyrite and stannite, thus pointing to the early, low-sulfidation assemblage as prospective for this *high-tech* metal in similar mineral systems. Indium was likely incorporated into the sphalerite crystal lattice via $Cu^+ + In^{3+} \leftrightarrow 2 Zn^{2+}$ and $(Sn, Ge)^{4+} + (Ga, In)^{3+} + (Cu + Ag)^+ \leftrightarrow 4 Zn^{2+}$ coupled substitutions. Indium incorporation mechanisms into the stannite and chalcopyrite crystal lattices remain unclear.

Keywords Indium · Critical metals · Central Andes · Cordilleran-type deposits · U–Pb cassiterite geochronology

Editorial handling: B. Lehmann.

Extended author information available on the last page of the article

Introduction

The Ayawilca Zn-Pb-Ag-In-Sn-Cu deposit hosts one of the largest resources among recent base-metal discoveries in central Peru and throughout the Andes. The project is located 40 km northwest of the historic Cerro de Pasco Zn-Ag-Cu mine, and 20 km northeast of the Uchucchacua Ag-Mn mine (Fig. 1). The overall resource at Ayawilca as of November 2018 stands at 11.7 Mt of indicated resources with grades of 6.9% Zn, 0.16% Pb, 15 g/t Ag, and 84 g/t In, equivalent to 983 t of contained In, assuming a 75% metallurgical recovery. Additionally, there are 45.0 Mt of inferred resources with grades of 5.6% Zn, 0.23% Pb, 17 g/t Ag, and 67 g/t In, using the same metallurgical assumptions. The project also hosts a separate Sn-Cu-Ag inferred resource of 14.5 Mt with grades of 0.63% Sn, 0.21% Cu, and 18 g/t Ag (Peralta et al. 2019).

Ayawilca was discovered by Tinka Resources Ltd. in 2012 following a scout drilling program aimed at a district target 2 km south of the Colquipucro sandstone-hosted Ag occurrence, where Tinka had focused its exploration efforts since staking the area in 2005. Zinc-rich mineralization, occurring as replacement bodies (mantos) in a Late Triassic–Early Jurassic carbonate sequence underlying the same gently dipping and unaltered Cretaceous sandstone unit that hosts Colquipucro, was identified and explored over the following years. The main mineralized base metal bodies are blind at Ayawilca. Thin east–west trending, Ag-rich veins with abundant Mn-Fe oxides cropping out over a few hundred meters in the exposed sandstone are the only surface evidence of the deposit. Initial drilling programs defined the West Ayawilca zone, with step-out drilling subsequently finding the Central Ayawilca and East Ayawilca zones. Following ground magnetics, airborne magnetics,

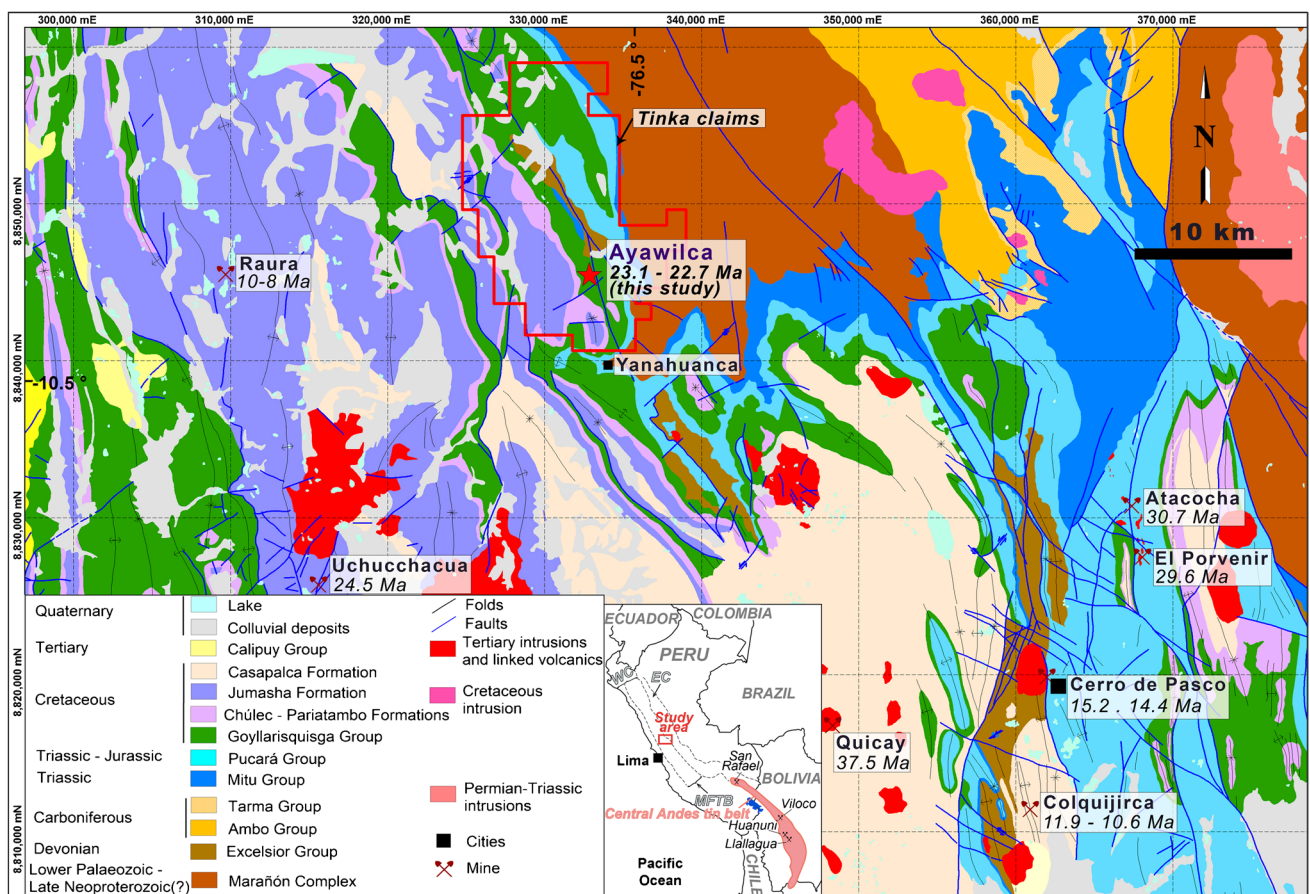


Fig. 1 Simplified geological map (modified from INGEMMET 1996, including data from Rosas et al. 2007, Bissig et al. 2008, Chew et al. 2016, and Spikings et al. 2016) showing the location of the Ayawilca and surrounding polymetallic deposits in central Peru. Approximate radiometric ages taken from summaries by Sillitoe and Perelló (2005)

and Bissig et al. (2008) except for the Cerro de Pasco and Colquijirca deposits, which are from Bendezú et al. (2008), Baumgartner et al. (2009), and Rottier et al. (2020). UTM zone 18S. Abbreviations: EC, Eastern Cordillera; MFTB, Marañón fold and thrust belt (MFTB); WC, Western Cordillera

and ground gravity surveys, the South Ayawilca and Zone 3 zones were discovered in 2017 and incorporated into the resource base (Fig. 2).

We show that Ayawilca has strong similarities with Cordilleran polymetallic deposits in central Peru as for example Morococha (Catchpole et al. 2015) and, in particular, Cerro

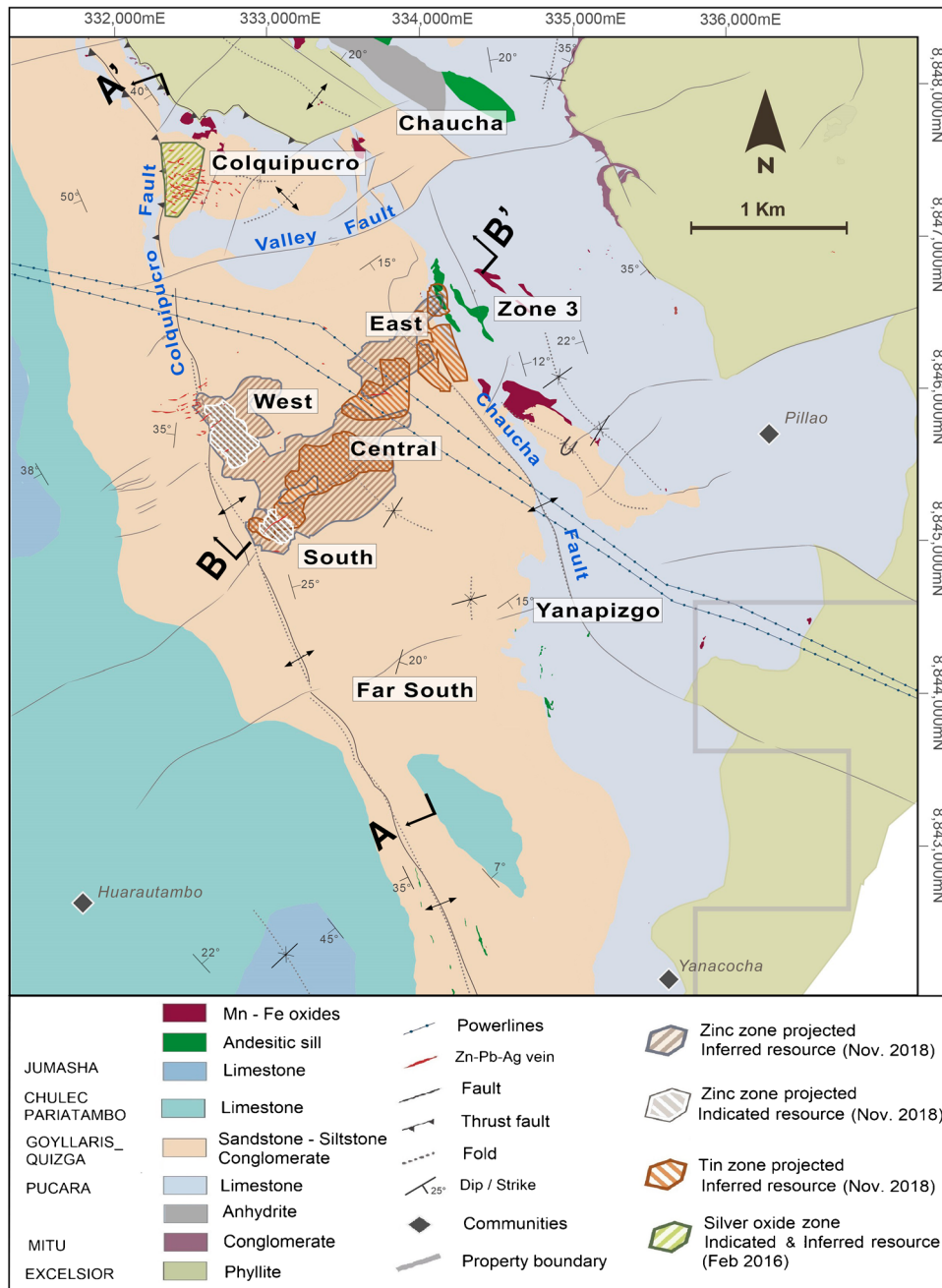


Fig. 2 Geological map of the study area showing the vertical surface projection of Zn, Ag, and Sn resources. A-A' (looking west) and B-B' (looking northwest) cross-sections across the Ayawilca deposit showing the location of the drill holes and metal grades. UTM Zone 18S. The NSR value was based on estimated metallurgical recoveries, assumed metal prices, and smelter terms, which include payable factors, treatment charges, penalties, and refining charges. Metal price assumptions were US\$1.15/lb Zn, US\$300/kg In, US\$15/oz Ag, US\$1.00/lb Pb, US\$9.00/lb Sn, and US\$2.85/lb Cu. Metal recov-

ery assumptions were 90% Zn, 75% In, 60% Ag, 75% Pb, 86% Sn, and 75% Cu. The NSR value for each block was calculated using the following NSR factors: US\$15.34 per % Zn, US\$4.70 per % Pb, US\$0.18 per gram In, and US\$0.22 per gram Ag, US\$155.21 per % Sn, and US\$37.59 per % Cu. The Zn NSR value was calculated using the formula $NSR = Zn(\%) * US\$15.34 + Pb(\%) * US\$4.70 + In(g/t) * US\$0.18 + Ag(g/t) * US\0.22 . The Sn NSR value was calculated using the following formula: $US\$NSR = Sn(\%) * US\$155.21 + Cu(\%) * US\$37.59 + Ag(g/t) * US\0.22

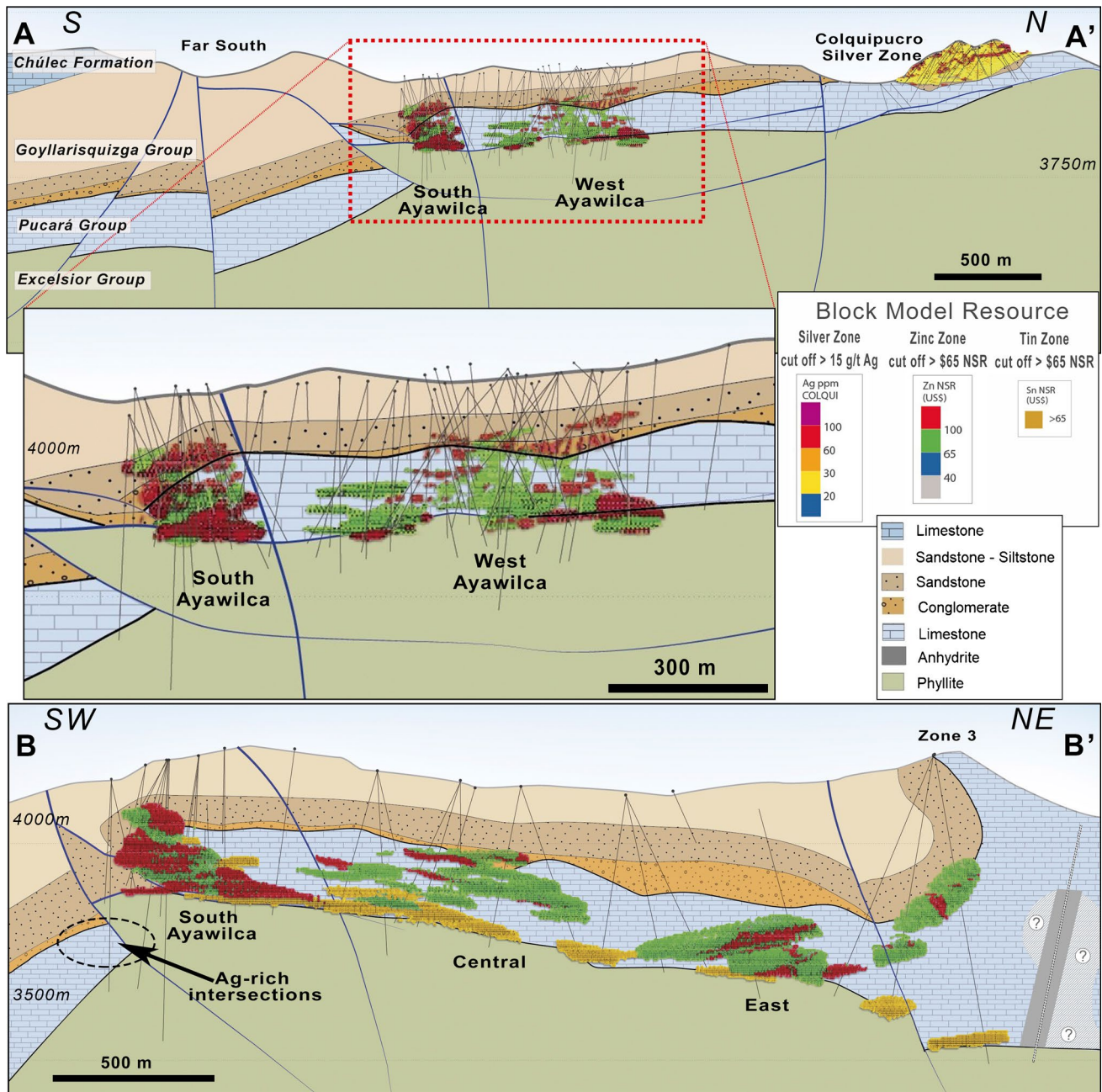


Fig. 2 (continued)

de Pasco (Baumgartner et al. 2008; Rottier et al. 2018). However, the area around Ayawilca was not considered prospective for deposits of this type because it lacked evidence of igneous activity or significant alteration zones, with the exception of that known at Colquipucro.

Indium is a significant component in the current resource at Ayawilca, which stands out as one of the largest undeveloped In resources in the world. Although In may form discrete minerals (e.g., roquesite [CuInS₂]), it mostly substitutes into the crystal lattice of sulfides, chiefly in sphalerite

(Schwarz-Schampera and Herzig 2002; Cook et al. 2009; Frenzel et al. 2014, 2016a, 2016b; Torr o et al. 2019a, 2019b), which explains its strong dependence on Zn production (Nassar et al. 2015). Other important In carriers include stannite (Torr o et al. 2019a, 2019b), chalcopyrite (Gaspar 2002; Andersen et al. 2016; George et al. 2016), and cassiterite (Pavlova et al. 2015; Lerouge et al. 2017; Gemrich et al. 2021).

The aim of this study is to describe the styles of mineralization, mineralogy, and mineral chemistry of the Ayawilca

deposit. Mineral textures are used to establish paragenetic sequences in replacement bodies and veins that serve to contextualize in situ EPMA and LA-ICP-MS trace element analyses of minerals, with special attention to the distribution of In. Additionally, we present the first direct dating of the Ayawilca mineralization, in accordance with which the formation of the deposit is placed within the metallogenic evolution of the central Andes. As a Sn- and In-bearing polymetallic deposit, the discovery, radiometric dating, and classification of the Ayawilca deposit are particularly significant for exploration focused on base and *high-tech* metals in the central Andes and elsewhere.

Regional geology and metallogenic setting

The Ayawilca deposit lies within the eastern part of the Marañón fold and thrust belt (MFTB), near its boundary with the basement high of the Eastern Cordillera (Fig. 1). The 1000-km-long NNW-SSE-trending MFTB constitutes the eastern part of the Western Cordillera of central to northern Peru (Mégard 1984; Benavides-Cáceres 1999; Eude et al. 2015; Piffner and Gonzalez 2013; Scherrenberg et al. 2016). It is the host for major ore deposits of Oligocene to Miocene age including Cu ± Mo ± Au porphyry, polymetallic and Cu-Fe skarn, epithermal precious and base metal deposits (e.g., Noble and McKee 1999; Scherrenberg et al. 2016; Fontboté 2018) that belong to “porphyry systems” as described by Sillitoe (2010).

The Marañón Complex (Wilson and Reyes 1964; Dalmayrac et al. 1988) refers historically to all metamorphic rocks in the Eastern Cordillera of Peru. This unit is composed of restricted domains potentially as old as late Neoproterozoic covered by Cambrian to Devonian low- to medium-grade metasedimentary rocks with volcanic intercalations, and is divided into two sub-units (Chew et al. 2007). The older sub-unit underwent metamorphism related to the Ordovician Famatinian orogeny, whereas the younger sub-unit underwent metamorphism related to the Carboniferous Gondwanian (formerly, Eo-Hercynian) orogeny (Chew et al. 2007, 2016; Cardona et al. 2009). The metasedimentary rocks of the Excelsior Group, the tentative Devonian age of which (McLaughlin 1924; Jenks 1951) is supported by osmium isotopic determinations consistent with an Eifelian age (Saintilan et al. 2021), represent the youngest unit of the metamorphic basement in the Eastern Cordillera. The Excelsior Group in central Peru is correlated with the Devonian Cabanillas Group in southern Peru (Rodríguez et al. 2011). Intrusions of I- and S-type granitoids took place during Ordovician, late Carboniferous, Permian, and Triassic magmatic events in the Eastern Cordillera (e.g., Chew et al. 2007, 2016; Mišković et al. 2009).

Carboniferous unmetamorphosed sandstones of the Ambo and Tarma Groups lie discordantly on the Marañón Complex and are unconformably overlain by the Triassic Mitu volcano-sedimentary sequence which includes interbedded alkaline lavas, red siliciclastic rocks, and polymictic conglomerates (McLaughlin 1924; Rosas et al. 2007; Spikings et al. 2016). The Mitu sequence shows large variations in thickness related to extensional faulting indicating deposition in a fault-controlled active rift basin (Rosas et al. 2007; Spikings et al. 2016). Rocks of the Mitu Group are locally absent (as at Ayawilca, see below) and regionally are overlain by the Late Triassic to Early Jurassic carbonate platform rocks of the Pucará Group deposited in the basin formed when the earlier rifts yoked together (Rosas et al. 2007). In central Peru, the Pucará Group is overlain by back-arc Early Cretaceous thick sandstone beds of the Goyllarisquizga Group (Wilson 1963; Scherrenberg et al. 2012). Albian to Maastrichtian sedimentary rocks, also deposited in a back-arc setting, include a transition from marine carbonates (Pariahuanca, Chulec, Pariatambo, and Jumasha Formations) to continental red sandstones and mudstones of the Casapalca formation (Wilson 1963; Jaillard and Arnaud-Vanneau 1993; Mégard et al. 1996; Benavides-Cáceres 1999). Basin inversion with east-vergent thin-skinned tectonics commenced in the Late Cretaceous (Peruvian to later Incaic phases of the Andean orogeny; Mégard 1984; Benavides-Cáceres, 1999; Eude et al. 2015; Scherrenberg et al. 2016) and was followed by west-vergent thick-skinned tectonics mainly from earliest Miocene (Scherrenberg et al. 2016).

The deformed sedimentary sequences were intruded by scattered late Eocene (ca. 40.2 Ma) to late Miocene (5.2 Ma) shallow-level calc-alkaline igneous stocks, mainly of granodioritic to rhyolitic composition (Bissig et al. 2008). Equivalent volcanic rocks occur mainly to the west of the study area. A magmatic lull is recognized in central Peru between 29.3 Ma and late Oligocene/early Miocene depending on the region. Extensive work, including abundant geochronological data, indicates that these shallow-level stocks are linked to porphyry and porphyry-related (in the sense of Sillitoe 2010) precious metal and polymetallic deposits that form a conspicuous NNW-SSE-trending belt in central and northern Peru (Noble and McKee 1999; Bissig et al. 2008; Fontboté 2018 and references therein). Most mineralization is of Miocene age and includes middle to late Miocene world-class deposits and districts as—from south to north—the Toromochu Cu-Mo porphyry deposit and the nearby polymetallic Domo de Yauli and Morococha districts, the polymetallic Colquijirca, Cerro de Pasco, and Antamina deposits, and the Yanacocha high-sulfidation gold deposit (Beuchat et al. 2004; Baumgartner et al. 2008; Bendežú and Fontboté 2009; Longo et al. 2010; Catchpole et al. 2015; Rottier et al. 2018; Mrozek et al. 2020). Middle to late Miocene mineralization

in central Peru coincided with a period of relatively flat subduction and decreasing magmatism subsequent to the subduction of the aseismic Nazca Ridge (Rosenbaum et al. 2005; Bissig et al. 2008; Scherrenberg et al. 2016). The Miocene belt in central and northern Peru is part of the Miocene-early Pliocene porphyry Cu belt recognized Andean wide (Sillitoe and Perelló 2005). In central Peru, the Miocene belt is partly superimposed on an older metallogenic belt of Eocene–Oligocene age that includes the Quicay, Atacocha, Uchucchacua, and Rondoní deposits, which are also parts of porphyry systems (Noble and McKee 1999; Sillitoe 2004; Bissig et al. 2008; Fontboté 2018; Fig. 1).

The Ayawilca deposit occurs in an area where the two metallogenic belts overlap. The lack of intrusive rocks in the area that could provide datable material had previously prevented assignment of the deposit to either the Eocene–Oligocene or Miocene belts.

Geology of the Ayawilca deposit

The Ayawilca Zn-Pb-Ag-In-Sn-Cu deposit lies within mineral concessions that cover an area of ~164 km² (Fig. 1). The main lithostratigraphic units occurring in the deposit area are the Devonian Excelsior Group, the Triassic-Jurassic Pucará Group, and the Cretaceous Goyllarisquizga Group (Fig. 2).

The Excelsior Group at Ayawilca consists mostly of organic-rich phyllite, composed of fine-grained muscovite and quartz as main minerals, and minor quartzite horizons. The rocks are foliated, locally brecciated, and contain abundant quartz veins. Although Mitu conglomerate-bearing red beds occur in the north of the study area (Fig. 2), at Ayawilca, the Pucará Group limestone overlies directly the Excelsior phyllite. The contact is interpreted to be faulted and is marked by a partly silicified tectonic breccia that consists of shard-like, imbricated quartz clasts derived from the phyllite (Gamarrá et al. 2019). The tectonic fabric is parallel to the contact, thus suggesting it is a low-angle shear fault.

The Pucará Group is the main host rock for the mineralization at Ayawilca and ranges typically between 150 and 200 m in thickness. The typical subdivision of the Pucará Group into three units, as commonly described in this part of Peru (see Rosas et al. 2007; Ritterbush et al. 2015), is not recognized at Ayawilca, perhaps because of the hydrothermal alteration that affected the rocks and/or the faulted contact with the underlying Excelsior Group rocks. The identified relict sedimentary facies at Ayawilca are bioclastic wackestones, peloidal packstones, and grapestones. Bivalves and corals are identified in the wackestones. Peloidal packstones include pellets or peloids with a laminar structure. These two facies probably correspond to a subtidal lagoonal environment. The grapestones include millimeter-sized grain

lumps (Fig. S1A). A body of massive anhydrite ± gypsum (at least 100-m thick) crops out in the northern part of the study area (Fig. 2). Massive anhydrite ± gypsum has also been intersected by drillholes in zone 3 (e.g., 536.7 m anhydrite ± gypsum intersected in hole A17-73, collar at 334459E 8846615 N). The evaporites cut with discordant brecciated subvertical contacts through the carbonate stratigraphy. The distribution suggests that the evaporites underlie the Pucará carbonate rocks or are interbedded in their lower part, as observed elsewhere (Rosas et al. 2007; Sempere and Acosta 2019), and in places have been subsequently diapirically deformed.

At Ayawilca, the carbonate rocks of the Pucará Group are dominantly dolomitic and display strong brecciation and subordinate chert. The breccias are either monolithic or heterolithic and most likely a product of dissolution due to hydrothermal activity. In the monolithic breccias, both the fragments and matrix are composed of dolomite. The heterolithic breccias are made up of siliceous fragments, predominantly quartz and quartz-arenites, within a dolomitic matrix (Fig. S1B). Pervasive dolomitization is finely to moderately crystalline, locally coarsely crystalline, resulting in a generalized obliteration of primary sedimentary features. The origin of this dolomitization can be diagenetic and/or hydrothermal. Microcrystalline quartz (chert) occurs as nodules that in places also show coarsely crystalline portions.

The Goyllarisquizga Group is empirically subdivided by geologists of Tinka Resources into three distinct clastic sedimentary sequences. The lowermost member, named Lower Goyllar, consists of conglomerates, sedimentary breccias, sandstones, black shales, and siltstones with an overall thickness between 10 and 70 m. Lying conformably above the Lower Goyllar unit is a quartz arenite member named Middle Goyllar. It is 50- to 70-m thick and consists of medium-grained, cross-bedded, and well-sorted quartz arenites. Its contact with the Lower Goyllar unit is gradational, coarsening upwards into thin conglomerate beds that are used as markers to determine the contact. The Upper Goyllar unit lies conformably on the Middle Goyllar unit, and its outcrops are abundant in the study area (Fig. 2). It includes sandstone, siltstone, and mudstone beds that are apparently unaltered (apart from incipient Mn-Fe oxide clots above the zones of mineralization), unmineralized, and undeformed. The Upper Goyllar is approximately 400-m thick in the southern part of the area.

The Ayawilca and Colquipucro deposits are bounded to the west by the NNW-SSE-striking Colquipucro fault (Fig. 2). The Colquipucro fault and other similarly oriented faults are cut by steep NEE-SWW-striking faults with which part of the mineralization is spatially associated with (Fig. 2). North of the NEE-SWW-striking Valle fault, near the Colquipucro Ag mineralization, the Colquipucro fault places the carbonate rocks of the Pucará Group over the

sandstones of the Goyllarisquizga Group; there, the Colquipucro fault shows east-verging thrusting (i.e., the typical vergence of the thin-skinned tectonics along the MFTB; Mégard 1984; Scherrenberg et al. 2016). The vergence of the Colquipucro fault south of the Valle fault could not be determined.

Drilling since 2017 in the western sector of Ayawilca identified several locations where phyllites of the Excelsior Group are thrust over the carbonate rocks of the Pucará Group along west-verging low-angle faults (Fig. 2, section B-B'). At South Ayawilca, several low-angle thrusts ramp up through the carbonate rocks of the Pucará Group to form a duplex. A moderately inclined and plunging anticline developed in the hanging wall of the roof thrust of the duplex. The core of this anticline is composed of carbonate rocks of the Pucará Group and hosts some of the highest grade and thickest mineralization found at Ayawilca. These west-verging thrust faults project close to the trace of the Colquipucro fault on surface (Fig. 2), but their vergence is at odds with the east vergence observed in this structure north of the Valley Fault. The west-verging faults and the Chaucha fault to the east define a basement high; east of it, the sedimentary sequence appears to be thicker and include the aforementioned thick evaporite unit and forms an overturned syncline (section B-B' in Fig. 2). The west-verging thrusting recognized at South Ayawilca may correspond to the west-verging thick-skinned event described by Scherrenberg et al. (2016).

The mineralization at Ayawilca occurs as replacement mantos and veins in the carbonate rocks of the Pucará Group and, to a lesser extent, in rocks of the Lower Goyllar unit (Fig. 2; Peralta et al. 2019). Quartz-sphalerite and massive sphalerite veins up to 1.3-m thick in the underlying Excelsior phyllites (Fig. S1C) are interpreted as feeders for the mineralized bodies. The sphalerite-bearing mantos in carbonate rocks of the Pucará Group are up to 30-m thick. Tin-copper mineralization occurs mostly within massive, 10- to 70-m-thick pyrrhotite replacement bodies at the base of the Pucará Group, particularly at Central Ayawilca (Fig. S1D), and in places is overprinted by the main Zn mineralization (Fig. S1E-F). Where the Pucará Group rocks are most deformed, particularly near the intersections of major faults and/or folds, the mantos can be stacked, and mineralization can be up to 200-m thick. Mineralization postdates the NNW-SSE-striking thrust faults and is in places affected by NEE-SWW-striking steep normal faults. No intrusive rocks have been found in outcrops nor in drill cores at the Ayawilca deposit. However, 3 km northeast of the East Ayawilca Zone, at about 3300 m.a.s.l., a granodiorite stock showing argillic alteration and pyrite veinlets crops out in an area of 300 x 200 m (Peralta et al. 2019). Minor andesitic dykes and sills in carbonate rocks of the Pucará Group (Fig. 2) are,

according to regional comparison, typical for Jurassic and Cretaceous subvolcanic activity unrelated to mineralization.

Sampling and analytical methods

The study is based on 60 representative core samples from mantos and veins in the Ayawilca deposit, which were collected from 24 drill holes. A list of the samples and their locations are provided in Table S1. A detailed description of the analytical methods is available in Appendix S1. A total of 42 thick polished sections were prepared at the QEM-SCAN laboratory of the Pontifical Catholic University of Peru (PUCP, Peru) for petrographic study under reflected-light polarizing microscope and SEM-EDS at the Centro de Caracterización de Materiales of the PUCP (CAM-PUCP). Mineralogical determinations, chiefly on hydrothermal alteration products, were carried out by X-ray diffraction (XRD; n = 24) at the CAM-PUCP. Results of XRD analyses are provided in Appendix S2.

Chemical compositions of sulfides, sulfosalts, and oxides were determined by means of electron microprobe (EPMA) and laser-ablation inductively coupled plasma mass spectrometry (LA-ICP-MS). EPMA analysis of sulfides, sulfosalts, and cassiterite was performed at the Centres Científics i Tecnològics of the University of Barcelona (CCiT-UB), and EPMA analysis of magnetite was performed at the Laboratorio Universitario de Petrología of the Instituto de Geofísica, Universidad Nacional Autónoma de México (UNAM). Lower limits of detection (L.O.D.), representative analyses of the different minerals investigated, and the normalization constants used for formula calculations are displayed in Table S2.

LA-ICP-MS analysis of sphalerite, chalcopyrite, and stannite was performed at ETH Zürich (Switzerland) and of magnetite at the Laboratorio de Estudios Isotópicos (LEI) of the Centro de Geociencias, UNAM. The list of analyzed isotopes and corresponding dwell times, the complete data set (content, uncertainties, and L.O.D.), and statistical data are provided in Table S3 (sulfides and sulfosalts) and Table S4 (magnetite). LA-ICP-MS analyses of cassiterite were carried out at ETH Zürich (trace element and U–Pb isotopic compositions; Table S5) and at the Southwest Isotope Research Laboratory of the US Geological Survey (USGS), Denver (U–Pb isotopic compositions; Table S6). Significant effort was made to avoid reporting mixed mineral analyses that result from the presence of nano- and micro-inclusions in the analyzed minerals. To accomplish this, we analyzed areas free of obvious inclusions and, during data processing, only selected smooth, constant signal segments in time-resolved ablation spectra for trace element quantification.

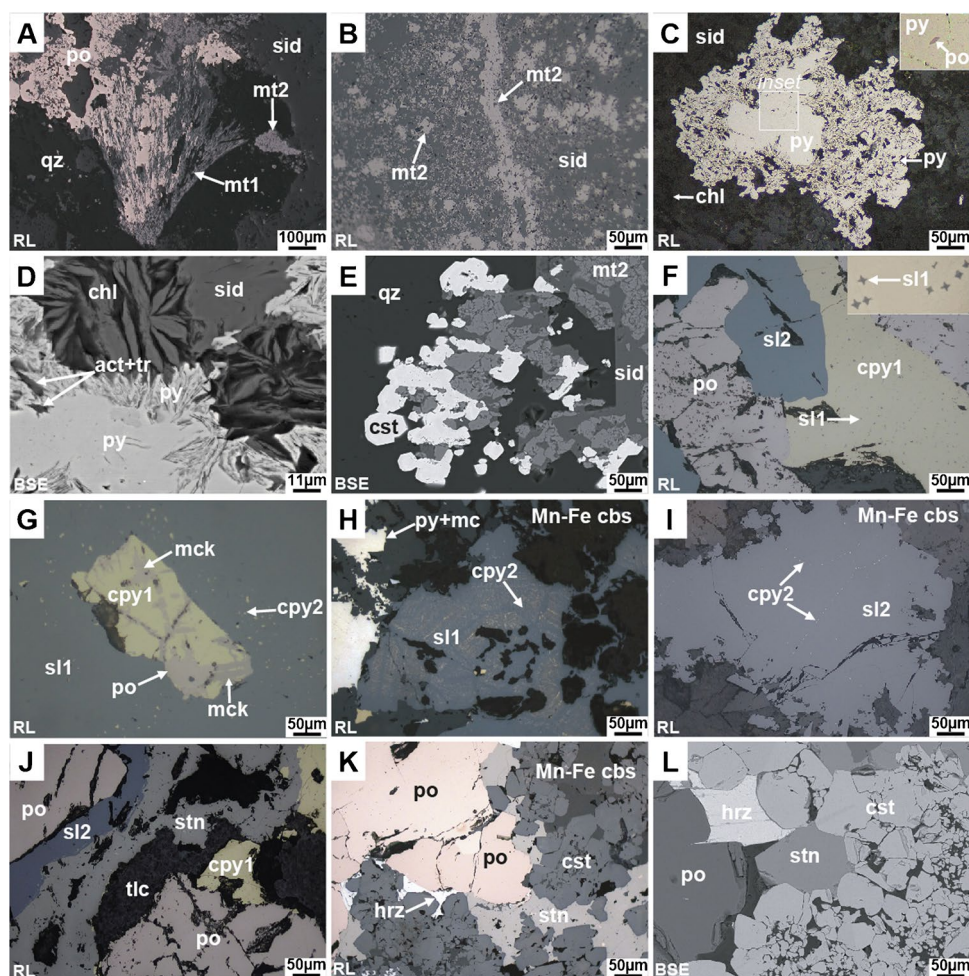


Fig. 3 Photomicrographs of textural features in manto mineralization in the Ayawilca deposit. **A** Magnetite as radial (1st generation) and fine (2nd generation) aggregates pervasively replaced by massive pyrrhotite and Mn-Fe carbonates. **B** Dense dissemination of magnetite (2nd generation) on a Mn-Fe carbonates matrix cut by a magnetite vein (3rd generation). **C**, **D** Zoned coarse pyrite with a massive core hosting small pyrrhotite inclusion, and irregular borders hosting acicular crystals of actinolite-tremolite in part replaced by chlorite. **E** Magnetite aggregates (2nd generation) in quartz matrix partially replaced by subhedral/anhydral cassiterite and siderite. **F** Massive pyrrhotite replaced by chalcopyrite (1st generation) with fine spherulite-star inclusions (1st generation), and massive, “clean” spherulite (2nd generation). **G** Chalcopyrite (1st generation) with oriented inclusions of tabular and lamellar mackinawite and irregular grains of pyrrhotite, in spherulite (1st generation) hosting blebs of chalcopyrite (2nd generation). **H** Spherulite (1st generation) with fine-grained, oriented chalcopyrite (2nd generation) inclusions, in contact with pyrite and fine-grained marcasite, the assemblage being partially replaced by Mn-Fe carbonates. **I** Spherulite (2nd generation) aggregates with very fine, low-density dissemination of chalcopyrite blebs (2nd generation). **J** Pyrrhotite and chalcopyrite (1st generation) cut by “clean” spherulite (2nd generation) and stannite. **K**, **L** Pyrrhotite intergrown with subhedral/euhedral cassiterite aggregates; stannite and herzenbergite occupy interstitial space. **M** Subhedral arsenopyrite crystals replaced by pyrite and marcasite. **N** Massive pyrrhotite partially replaced by an assemblage of fine-grained pyrite, marcasite, and intermediate product, the whole assemblage being replaced by

Mn-Fe carbonates. **O** Sphalerite (2nd generation) and arsenopyrite crystals pervasively replaced by pyrite and marcasite. **P** Interstitial spherulite (1st generation), pyrite, and marcasite within idiomorphic quartz aggregate; sphalerite hosts a fine dissemination of chalcopyrite (2nd generation). **Q** Sphalerite crystal with pyrite-marcasite rims and replaced by Mn-Fe carbonates. **R** Sphalerite (1st generation) with dissemination of chalcopyrite (2nd generation) and replacement of chalcopyrite (3rd generation) and Mn-Fe carbonates. **S** Arsenopyrite crystals with porosity, microfractures, and contacts lined with Fe-poor spherulite (3rd generation) and Mn-Fe carbonates. **T** Chalcopyrite (1st generation) replaced by spherulite (2nd generation), tetrahedrite-group minerals and Mn-Fe carbonates. **U** Sphalerite (2nd generation) with polymineral inclusion of argentian tetrahedrite, the latter with relicts of sphalerite (1st generation) with dissemination of chalcopyrite (2nd generation) and pyrrhotite. **V** Sphalerite (2nd generation) with inclusions of chalcopyrite (3rd generation), argentian tetrahedrite and pyrrargyrite. **W** Corroded arsenopyrite with galena inclusions. **X** Massive pyrrhotite with secondary porosity lined with native bismuth and bismuthiferous galena. Abbreviations: 1, 2, 3, first, second, and third generations; act-tr, actinolite-tremolite; aspy, arsenopyrite; Bi, native bismuth; Bi_{gn}, bismuthiferous galena; chl, chlorite; cpy, chalcopyrite; cst, cassiterite; Mn-Fe cbs, Mn-Fe carbonates; gn, galena; hrz, herzenbergite; I.P., intermediate product; mck, mackinawite; mc, marcasite; mt, magnetite; po, pyrrhotite; py, pyrite; pyrg, pyrrargyrite; qz, quartz; sid, siderite; sl, spherulite; stn, stannite; td_Ag, argentian tetrahedrite; tlc, talc; RL, reflected light image; BSE, backscattered electron image

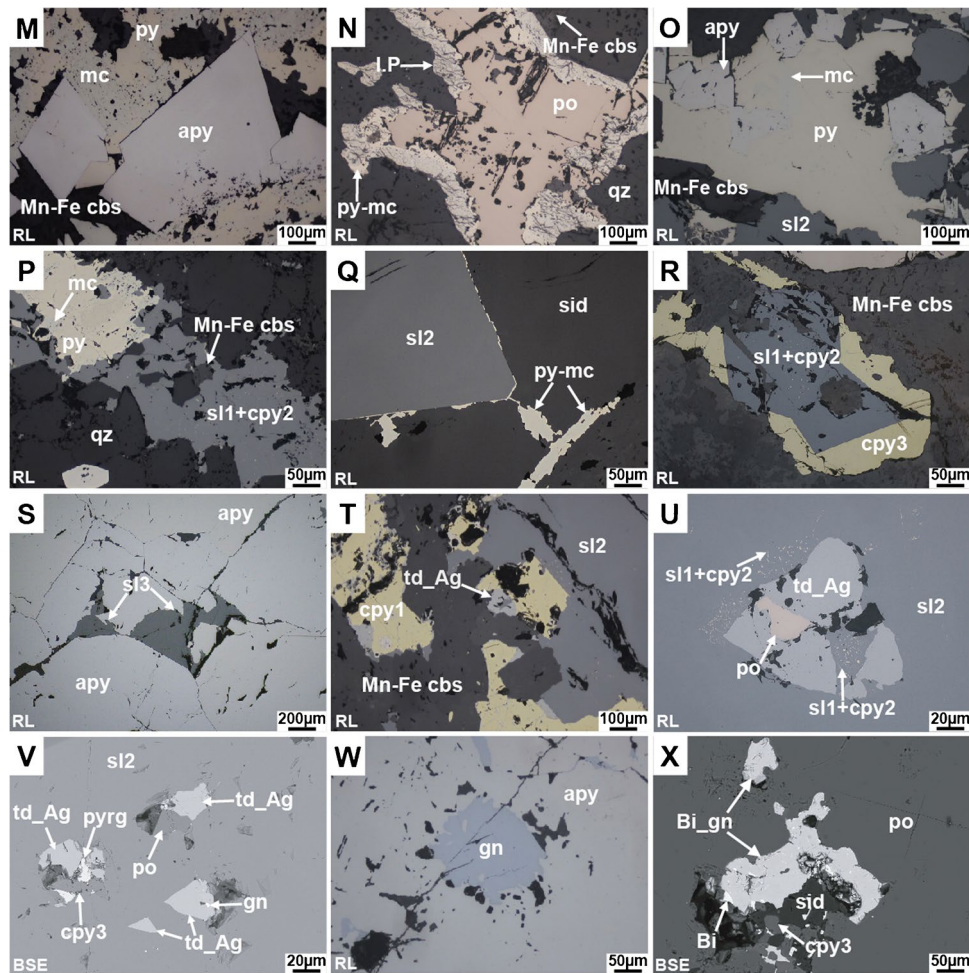


Fig. 3 (continued)

Hydrothermal alteration and mineralization

Mineral assemblages and paragenetic sequences in both mantos and veins define three main stages of evolution (stages A, B, and C; Figs. 3 and 4 and Fig. S2), similar to those recognized by Rottier et al. (2016, 2018) in the Cerro de Pasco deposit, as well as in other Cordilleran-type polymetallic deposits (Fontboté 2020). In addition, relicts of a magnesian retrograde skarn that predated stage A chiefly comprise Mg-siderite + talc + magnetite (Fig. S2A). Cassiterite mineralization, which also predates stage A, is only found in the deepest mantos, close to the contact between rocks of the Pucará and Excelsior Groups. The mineralization formed during stage A is the economically and volumetrically most important at Ayawilca, and is composed of a low-sulfidation assemblage of arsenopyrite, pyrrhotite, chalcocopyrite, Fe-rich sphalerite, stannite, and herzenbergite [SnS] (Fig. S2B–E). Stage A minerals are frequently overprinted by coarse pyrite that forms the bulk of stage B

(Fig. S2F). Stage C comprises an intermediate-sulfidation assemblage, mainly constituted by sphalerite, chalcocopyrite, galena, Cu–Ag sulfosalts, kaolinite, dickite, and carbonates (including siderite and intermediate compositions between rhodochrosite, siderite, and kutnohorite end-members, henceforth referred to as Mn–Fe carbonates). Stage C overprinted the assemblages of both stages A and B (Figs. S2G–I). The paragenetic sequences for mantos and polymetallic veins are summarized in Fig. 5.

Mantos

Hypogene metallic minerals in the mantos at Ayawilca include magnetite, pyrrhotite, arsenopyrite, sphalerite, chalcocopyrite, pyrite, marcasite, and lesser amounts of cassiterite, stannite, herzenbergite, mackinawite, tetrahedrite, galena, native bismuth, zoubekite [AgPb₄Sb₄S₁₀], stephanite, pyrrargyrite, and intermediate product (defined as a transition of pyrrhotite to marcasite and pyrite; Ramdohr 1969).

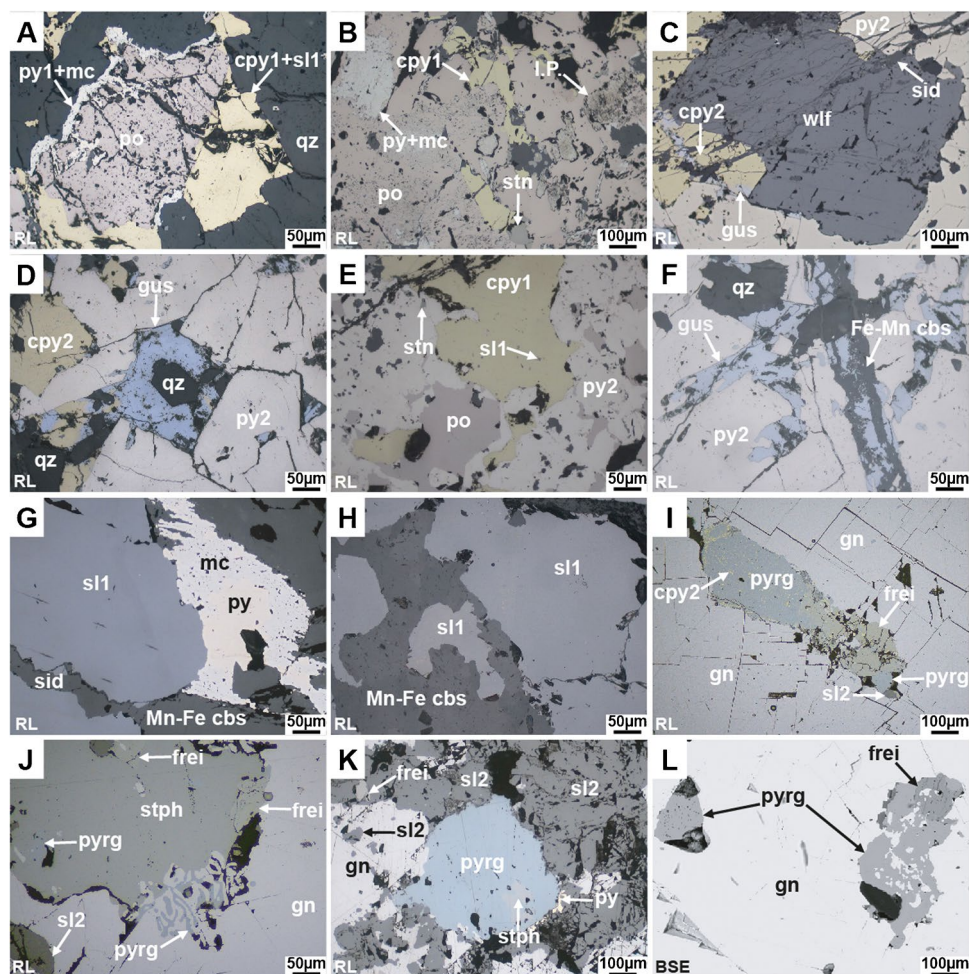


Fig. 4 Photomicrographs of textural features of veins in NE (A–F) and NW (G–L) Ayawilca deposit. **A** Pyrrhotite in interstices of quartz, replaced by chalcopyrite (1st generation) with fine inclusions of sphalerite “stars” (1st generation) and with pyrite and marcasite rims. **B** Corroded pyrrhotite replaced by a fine-grained assemblage of pyrite, marcasite, and intermediate product. Chalcopyrite (1st generation) and stannite vein pyrrhotite. **C** Medium-grained wolframite within a pyrite aggregate partially replaced by chalcopyrite (2nd generation) and gustavite; the whole assemblage is cut by fine veinlets of siderite. **D** Pyrite aggregates replaced by chalcopyrite (2nd generation) and gustavite. **E** Chalcopyrite (1st generation) with inclusions of sphalerite “stars,” and pyrrhotite replaced by pyrite (1st generation). **F** Pyrite vein (2nd generation) with inclusions of quartz and replaced by gustavite. **G–H** Sphalerite (1st generation) replaced by pyrite,

marcasite, siderite, and Mn-Fe carbonates. **I** Galena with secondary porosity and microfractures lined with sphalerite (2nd generation), chalcopyrite (3rd generation), freibergite, and pyrrargyrite. **J** Stephanite, with inclusions of freibergite and pyrrargyrite, is intergrown with galena; note the myrmekitic texture involving galena and pyrrargyrite. **K** Galena and finely intergrown pyrrargyrite and freibergite line porosity in corroded sphalerite (2nd generation). **L** Secondary porosity in galena is lined with pyrrargyrite and freibergite. Abbreviations: 1, 2, 3, first, second, and third generations; cpy, chalcopyrite; Mn-Fe cbs, Mn-Fe carbonates; frei, freibergite; gn, galena; gus, gustavite; mc, marcasite; po, pyrrhotite; py, pyrite; pyrg, pyrrargyrite; qz, quartz; sid, siderite; sl, sphalerite; stn, stannite; stph, stephanite; td_Ag, argentian tetrahedrite; wlf, wolframite; RL, reflected light image; BSE, back-scattered electron image

The deepest mantos are locally enriched in Mg-siderite, magnetite, talc, and cassiterite. Two generations of magnetite have been identified. The first occurs as pseudo-radial aggregates, probably as a replacement of < 600- μ m-long acicular amphibole crystals (Fig. 3A). The second generation comprises disseminated octahedral crystals with sizes that range between 800 and 120 μ m and < 125- μ m-thick stringers (Fig. 3B). Small laths of

actinolite–tremolite that were mostly replaced by chlorite occur shielded by pyrrhotite that was, in turn, massively replaced by pyrite (Fig. 3C, D). The amphiboles are interpreted as being part of a magnesian retrograde skarn formed prior to the main stage A sulfide assemblage along with Mg-siderite, magnetite, and talc, as a “pre-A stage” (Fig. 3A–C). Anhedral to subhedral cassiterite crystals up

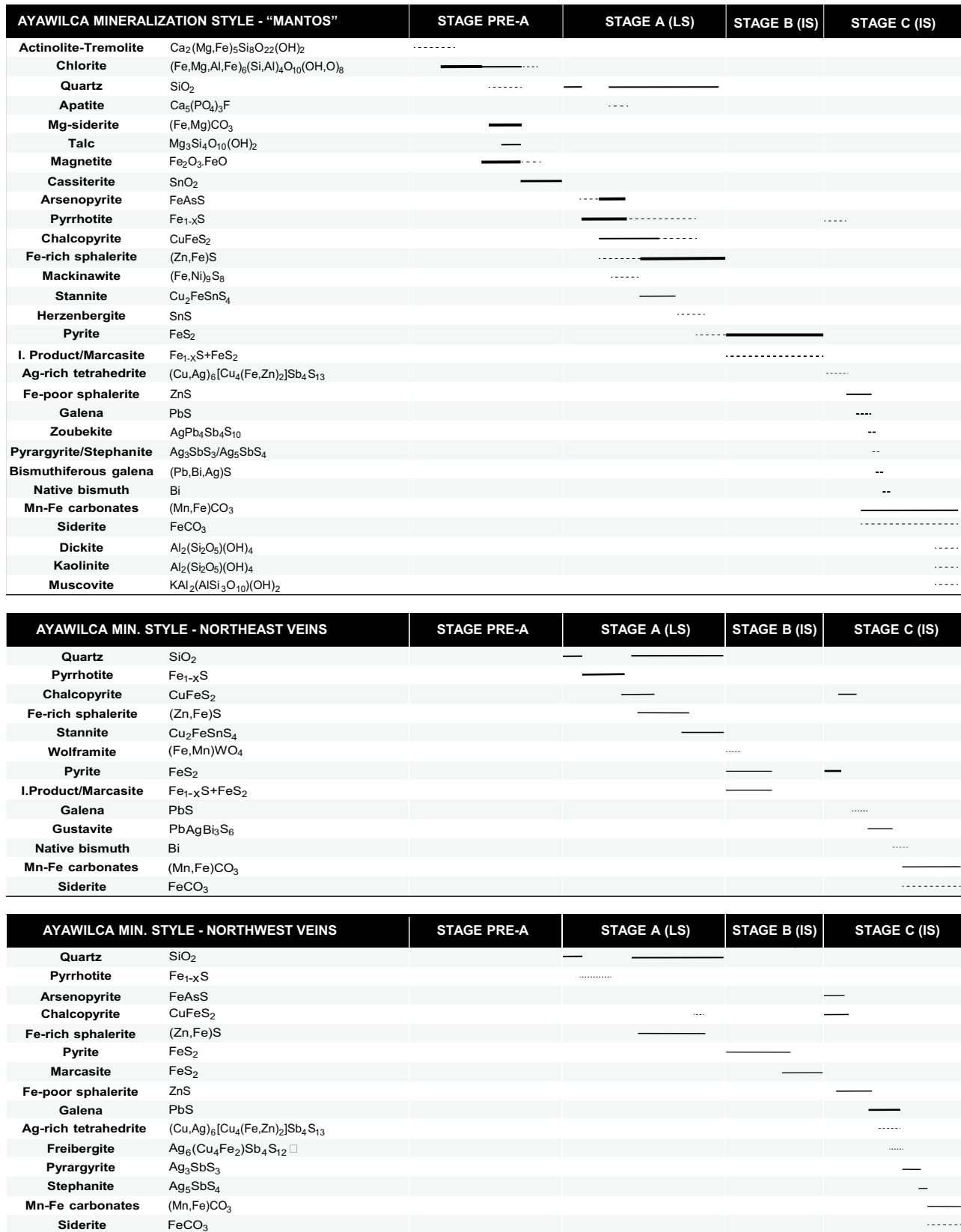


Fig. 5 Paragenetic sequence of mantos and polymetallic veins in Ayawilca. Thick bars indicate higher abundance and dashed lines lesser abundance

to 150 μm in size occur as a replacement of or filling interstitial space between magnetite grains (Fig. 3E).

Stage A in mantos comprises early prismatic quartz, massive pyrrhotite, and subhedral arsenopyrite followed by chalcopyrite, Fe-rich sphalerite, stannite, and herzenbergite. Two generations of Fe-rich sphalerite are observed. The first occurs both as star-shaped inclusions ($< 4 \mu\text{m}$) in massive, first-generation chalcopyrite (Fig. 3F) and as anhedral to subhedral crystals with fine-grained disseminations of second-generation chalcopyrite (Fig. 3G, H). First-generation chalcopyrite occasionally hosts lamellar mackinawite (Fig. 3G). Second-generation sphalerite shows clean surfaces and local, low-density, very fine chalcopyrite disseminations (Fig. 5I). Both Fe-rich sphalerite and first-generation chalcopyrite replaced massive pyrrhotite and were partially replaced, in turn, by rimming stannite (Fig. 3J). Stannite also occurs in the interstices of short, prismatic subhedral cassiterite crystals ($< 160 \mu\text{m}$). Herzenbergite ($< 620 \mu\text{m}$) occupies interstitial space between subhedral cassiterite and stannite and corroded pyrrhotite crystals (Fig. 3K, L).

During stage B, pyrite and quartz replaced both the carbonate rocks of the Pucará Group and stage A sulfides, mainly arsenopyrite (Fig. 3M), pyrrhotite (Fig. 3N), and Fe-rich sphalerite (Fig. 3O–Q). In the particular case of pyrrhotite replacement, pyrite is often intergrown with fine-grained marcasite and intermediate product (Fig. 3N).

During stage C, a third generation of chalcopyrite and Fe-poor sphalerite along with galena, and lesser amounts of tetrahedrite, native bismuth, bismuthiferous galena, pyrrargyrite, stephanite, and zoubekite are introduced. Third-generation chalcopyrite is observed as a replacement of Fe-rich sphalerite (Fig. 3R). Stage C sphalerite, which shows yellowish-brown internal reflections, occurs locally lining cavities in corroded arsenopyrite crystals (Fig. 3S). Locally, tetrahedrite is observed as a replacement of first-generation chalcopyrite (Fig. 3T). Traces of tetrahedrite (Fig. 3U), pyrrargyrite (Fig. 3V), and stephanite typically appear lining fine pores in stage A second-generation sphalerite. Galena occurs lining pores and microfractures in arsenopyrite (Fig. 3W) and sphalerite, and is locally replaced by zoubekite. Native bismuth and bismuthiferous galena occur in secondary pores in pyrrhotite, arsenopyrite, and Fe-rich sphalerite (Fig. 3X).

Veins

Veins in NE Ayawilca (Fig. 2) display similar mineralogy and micro-textural relationships to those ascribed to stages A and B in the mantos. The veins are mainly formed by comb quartz crystals between which available interstitial space is occupied by stage A massive pyrrhotite and first-generation chalcopyrite with star-shaped inclusions of

sphalerite (Fig. 4A, B). In contrast to the mantos, prismatic wolframite grains $< 1800 \mu\text{m}$ across occur locally in these veins (Fig. 4C). In some areas, both pyrrhotite and first-generation chalcopyrite were partially replaced by stannite and Fe-rich sphalerite, and the whole assemblage, in turn, by stage B pyrite, intermediate product, and marcasite. Pyrite is also observed forming aggregates of anhedral to subhedral microfractured crystals, with interstices and porosity lined with stage C native bismuth ($< 30 \mu\text{m}$), galena ($< 150 \mu\text{m}$), and gustavite [$\text{AgPbBi}_3\text{S}_6$] ($< 350 \mu\text{m}$; Fig. 4D–F), and cut by fine veinlets of siderite and Mn–Fe carbonates. A second generation of chalcopyrite (stage C) characterized by absence of mineral inclusions is observed lining microfractures in pyrite and overprinting first-generation chalcopyrite.

Veins in NW Ayawilca (Fig. 2) mainly consist of sphalerite, galena, Ag–Cu sulfosalts, pyrite, and lesser amounts of arsenopyrite, marcasite, pyrrhotite, and chalcopyrite. Two generations of chalcopyrite have been identified: the first occurs as fine disseminations ($< 4 \mu\text{m}$) on first-generation sphalerite (stage A), and the second forms anhedral crystals (stage C). Stage A sphalerite, which is Fe-rich, presents reddish-brown internal reflections and hosts also small inclusions of pyrrhotite. First-generation sphalerite was replaced by stage B pyrite/marcasite and stage C siderite and Mn–Fe carbonates (Fig. 4G, H). First-generation sphalerite and stage C second-generation chalcopyrite were replaced by, and its porosity lined with galena, Ag–Cu sulfosalts (tetrahedrite, freibergite, stephanite, and pyrrargyrite; all $< 600 \mu\text{m}$ across) and a second generation of sphalerite with light yellow internal reflections (Fig. 4I–L). Symplectic intergrowths involving galena, pyrrargyrite, and freibergite (Fig. 4J, L) are observed.

Mineral geochemistry

Summaries of the compositions, including minimum, maximum, average, and interquartile range (IQR) values for sphalerite, stannite, and chalcopyrite are reported in Table S3, for magnetite in Table S4, and for cassiterite in Table S5. Additionally, LA-ICP-MS analyses of sphalerite are presented in compiled box-and-whisker plots (Fig. 6 and Appendix S3). Trace elements will be henceforth reported as IQR unless otherwise specified.

Sphalerite

Sphalerite grains from the Ayawilca deposit yield a relatively broad compositional spectrum. In mantos, Fe contents are generally higher in stage A sphalerite, both in the first and second generations (14.1–11.5 wt%), and much lower

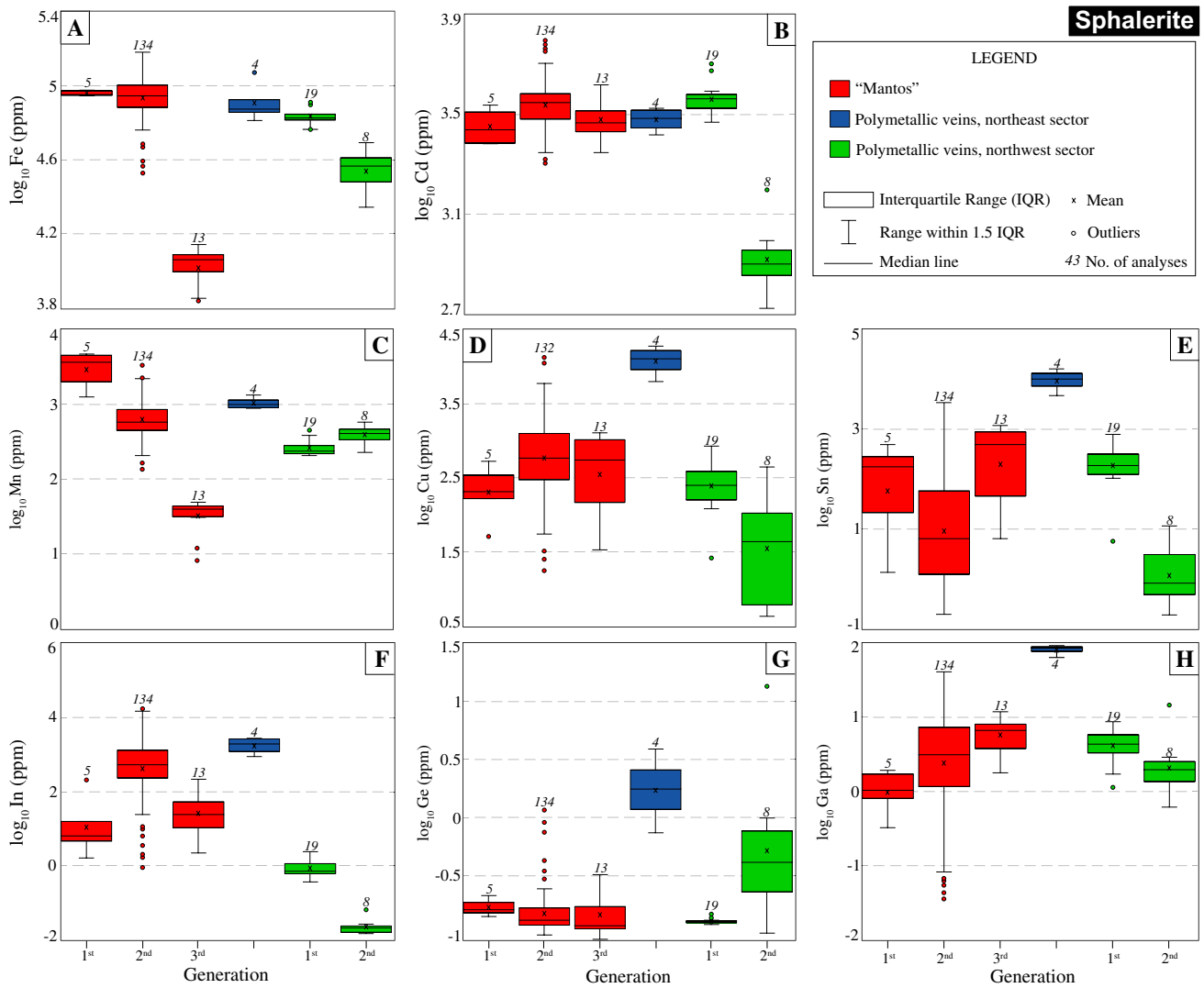


Fig. 6 Selected boxplots of log-transformed element contents in sphalerite from the Ayawilca deposit (LA-ICP-MS data)

in grains of the third generation (stage C; 2.4–2.0 wt%). Iron values are normally higher in sphalerite from NE Ayawilca (10.8–10.3 wt%) than in NW Ayawilca, which records Fe depletion from first (14.4–5.3 wt%, stage A) to second generations (4.7–4.0 wt%, stage C; Fig. 6A). Zinc tends to have a fairly negative correlation with Fe (Fig. 7A), thus pointing to a dominant $Fe^{2+} \leftrightarrow Zn^{2+}$ simple isovalent substitution.

Cadmium values are relatively constant in all analyzed sphalerite grains from mantos (3823–2417 ppm) and veins at the NE sector (3828–2672 ppm; Fig. 6B). In veins from the NW sector, Cd content is much higher in sphalerite grains of the first generation (3818–3329 ppm, stage A) than in those of the second generation (955–698 ppm, stage C). Manganese content in sphalerite from mantos decreases steadily from grains of the first generation (4635–1623 ppm) to those of the second (870–452 ppm, stage A) and third (45–31 ppm,

stage C) generations (Fig. 6C). In contrast, sphalerite from veins at NW Ayawilca records a subtle increase in the Mn content from grains of the first (295–218 ppm, stage A) to grains of the second (486–312 ppm, stage C) generations. Cadmium shows a weak negative correlation with Zn (Fig. 7B) and a strong positive correlation with Fe (Fig. 7C). Iron is also positively correlated with Mn (Fig. 7D), thus suggesting more complex isovalent substitution mechanisms of Zn^{2+} for Fe^{2+} , Cd^{2+} , and Mn^{2+} (see Graeser 1969; Cook et al. 2009; Pring et al. 2020).

Copper content in sphalerite from mantos (1273–108 ppm) is higher in grains of the stage A second generation (1273–281 ppm) relative to those of the first (438–108 ppm) and stage C third (1059–127 ppm) generations (Fig. 6D). As for sphalerite in veins, Cu content is higher in grains from the NE sector (18,337–7373 ppm) than

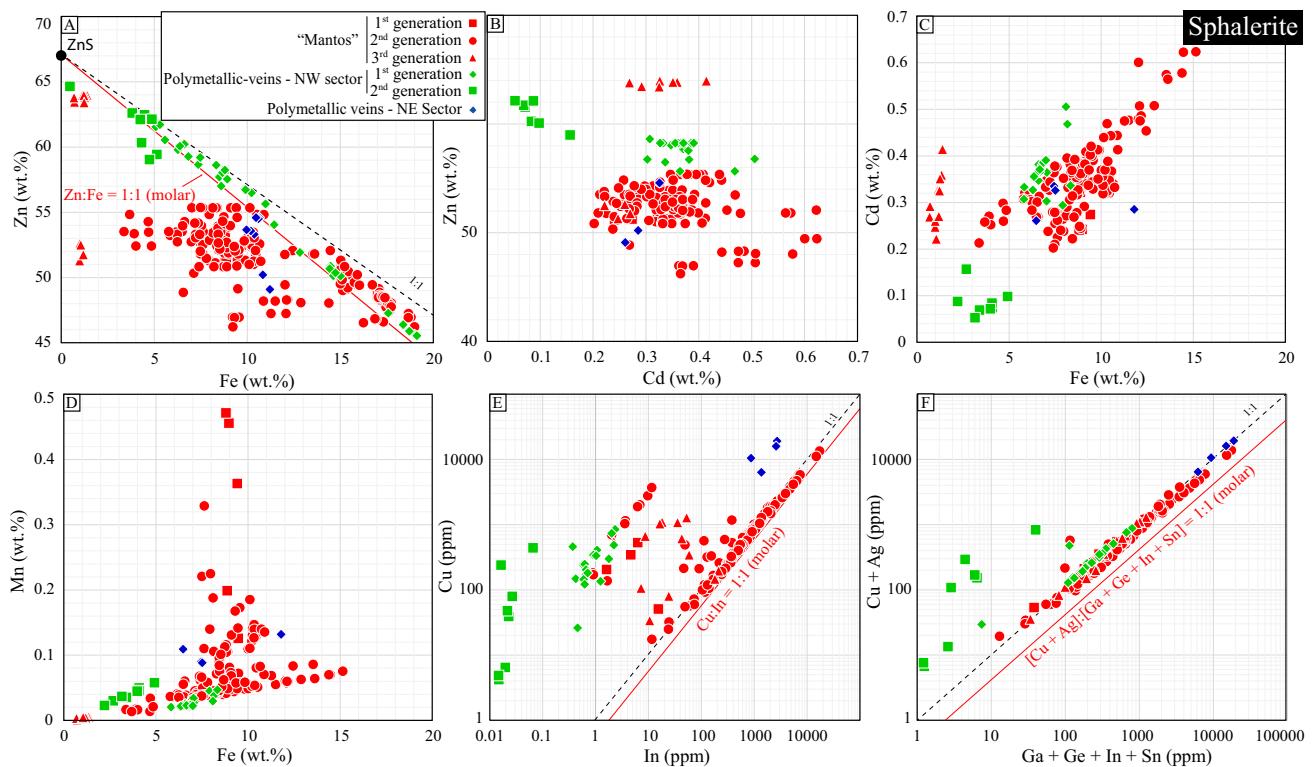


Fig. 7 Correlation between elements in sphalerite from the Ayawilca deposit (LA-ICP-MS data)

in those from the NW sector (408–6 ppm). In veins from the NW sector, there is a drastic depletion in Cu from first- (408–148 ppm, stage A) to second-generation (239–6 ppm, stage C) sphalerite. Copper normally shows very good correlations with other minor and trace elements (e.g., In, Ag, and Sn), thus suggesting that Cu was incorporated within the crystal lattice of sphalerite through coupled substitutions (Fig. 7E, F; further discussed below).

Tin content is markedly variable according to both the mineralization style and the sphalerite generation (Fig. 6E). The highest Sn contents are recorded in sphalerite grains from veins at NE Ayawilca (15,100–5667 ppm). In veins at NW Ayawilca, a trend towards Sn depletion from early (336–125 ppm) to late (3.3–0.48 ppm) sphalerite generations is observed. In contrast, sphalerite grains from mantos show an irregular content, with general depletion in the second generation (59–1.2 ppm, stage A) relative to the first (386–11 ppm, stage A) and third (929–43 ppm, stage C) generations. Silver content is highest in sphalerite from veins at NE Ayawilca (195–110 ppm) and relatively constant in veins at NW Ayawilca (41–2.6 ppm) and mantos (30–3.3 ppm). Much lower are the values of Hg, which increase from the first (1.4–1.1 ppm) to the second (2.1–1.4 ppm, stage A) and third (32–17 ppm, stage C) sphalerite generations in mantos and from the first (3.2–2.6 ppm, stage A) to the

second (50–22 ppm, stage C) generations in veins from NW Ayawilca.

Among critical elements (In, Ge, Ga), the highest contents in analyzed sphalerite from Ayawilca are those of In (986–16 ppm, up to 1.7 wt%). In mantos, this element is more abundant in second-generation (1299–227 ppm, stage A) than in first- (109–3.1 ppm, stage A) and third-generation (56–9.6 ppm, stage C) sphalerite (Fig. 6F). Sphalerite from veins at NE Ayawilca yields much higher In contents (2676–993 ppm) than sphalerite from veins at NW Ayawilca (up to 1.2 ppm). In the latter, there is an In depletion trend from first- (1.2–0.6 ppm, stage A) to second-generation (<0.10 ppm, stage C) sphalerite (Fig. 6F). Germanium contents are systematically low (0.24–0.14 ppm, up to 14 ppm; Fig. 6G) but slightly higher in veins from NE Ayawilca (3.5–0.90 ppm). Gallium values in sphalerite from both mantos and veins are mostly a few ppm but slightly higher in grains from veins at NE Ayawilca (91–69 ppm, up to 92 ppm; Fig. 6H). In mantos, there is a subtle increase in the Ga content from first- (1.8–0.57 ppm) to second- (7.3–1.2 ppm, stage A) and third-generation (8.7–3.7 ppm, stage C) sphalerite. Element correlations and substitution mechanisms of In, Ge, and Ga in sphalerite are addressed in detail in the “Discussion” section.

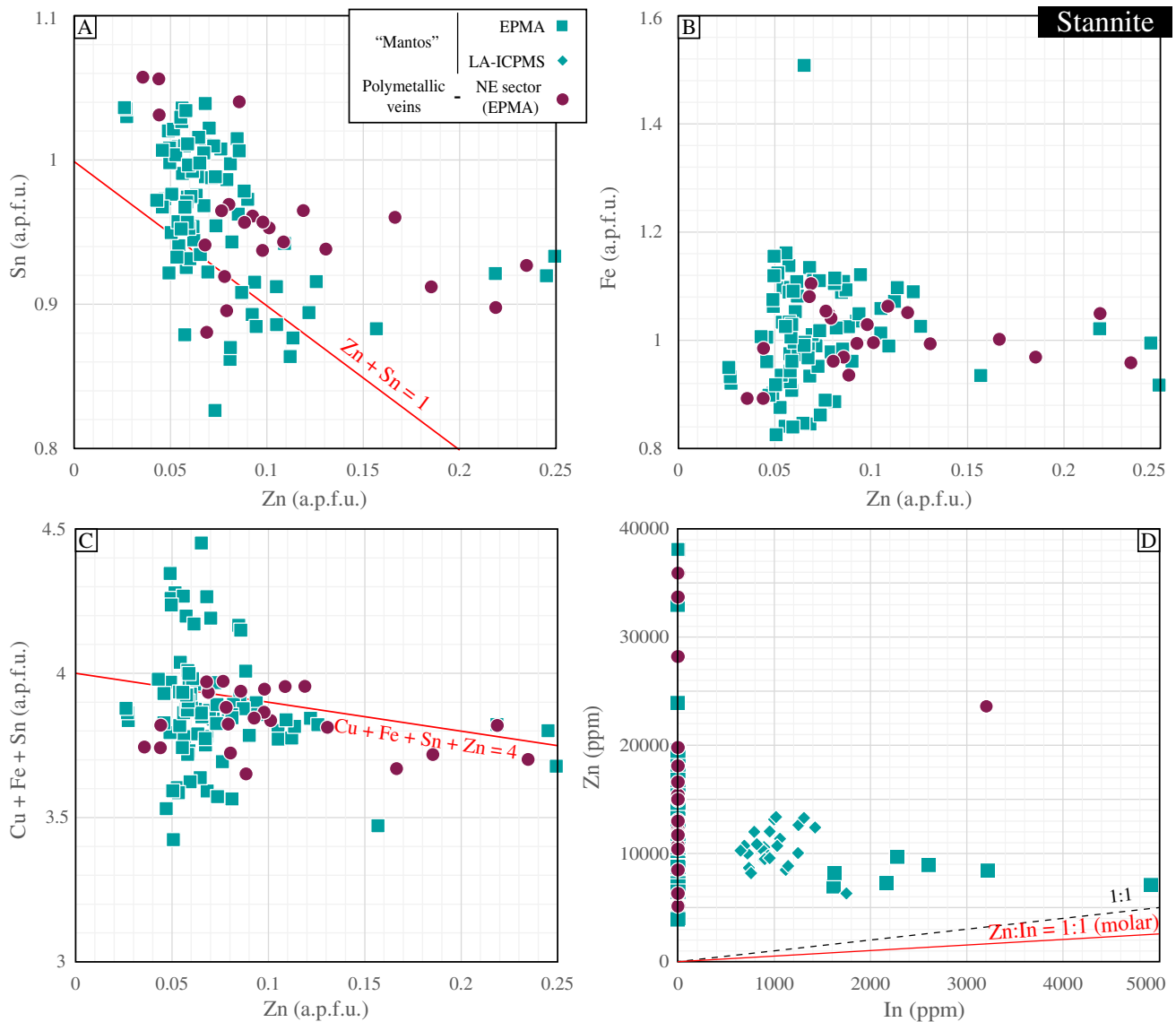


Fig. 8 Correlation between elements in stannite from the Ayawilca deposit (A–C EPMA data; D LA-ICP-MS data)

Stannite group minerals

Our EPMA and LA-ICP-MS datasets for stannite group minerals from the studied mantos reveal a narrow compositional range for Cu (28.9–26.3 wt%), Sn (26.8–25.8 wt%), and Fe (13.8–11.9 wt%), and relatively high Zn (12,025–9315 ppm) and Ag (1623–1360 ppm). Indium content in stannite from mantos is significant (1168–869 ppm; up to 1908 ppm), whereas the contents of Ga and Ge are much lower (both, < 20 ppm). Analyzed stannite grains yield Zn/(Fe + Zn) atomic ratios between 0.03 and 0.24. As Zn tends to have a subtle negative correlation with Sn (Fig. 8A) and does not show a negative correlation with Fe (Fig. 8B), a governing role for the stannite-k esterite solid solution series in the composition of studied stannite is

excluded. In contrast, the negative correlation between Zn and Cu + Fe + Sn at $Zn + Cu + Fe + Sn \sim 4$ a.p.f.u. (Fig. 8C) suggests that the incorporation of Zn can be contextualized within a solid solution between stannite and (Fe-rich) sphalerite (see Oen et al. 1980).

Chalcopyrite

Chalcopyrite grains from mantos and NE Ayawilca veins were analyzed. Iron content is relatively constant (29.9–29.0 wt%) whereas the contents of Sn, Ag, and Cd are considerably higher in vein (4204–3380 ppm Sn, 962–665 ppm Ag, and 31–15 ppm Cd) than in manto (2278–1715 ppm Sn, 402–336 ppm Ag, and 5.8–2.8 ppm Cd) chalcopyrite. Indium values are higher in stage A first-generation

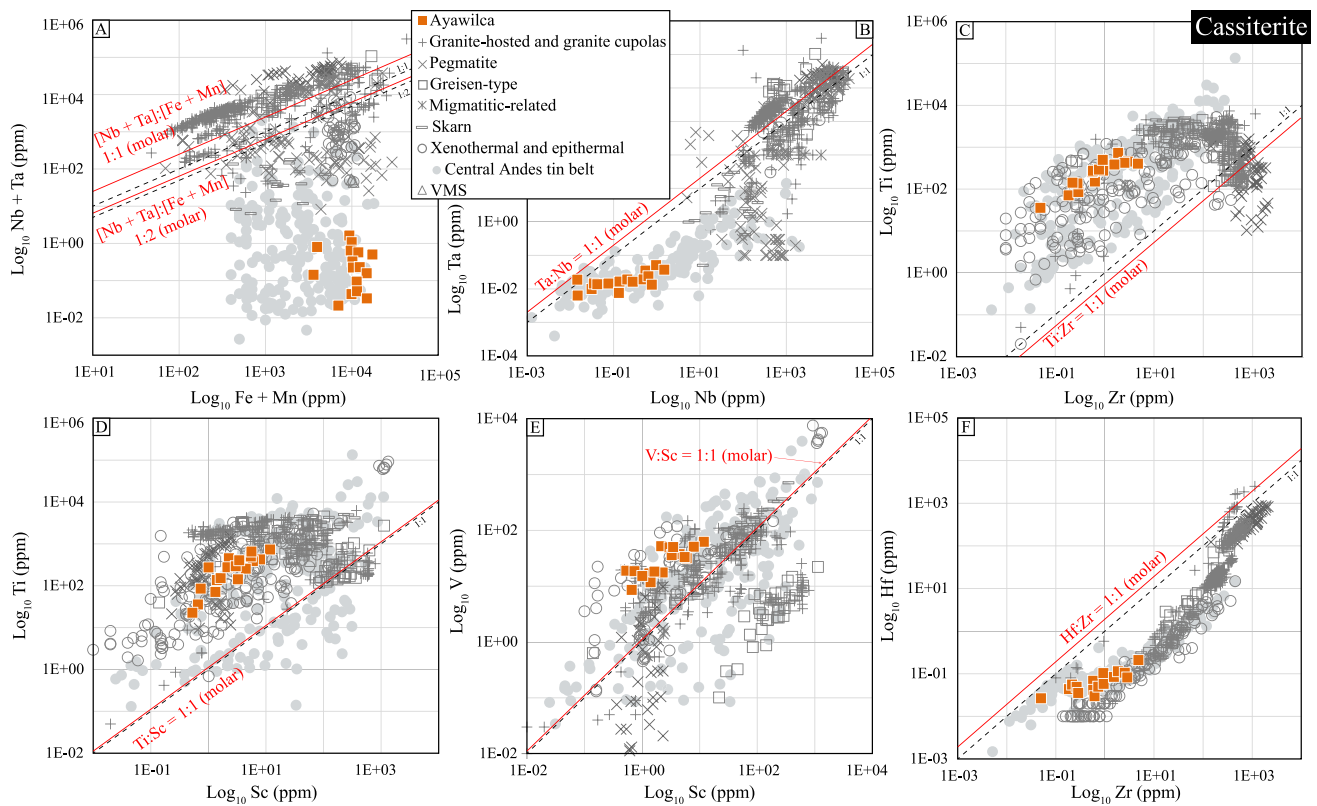


Fig. 9 Correlation binary plots for Ayawilca cassiterite (LA-ICP-MS data). Reference data are shown for comparison (Moore and Howie 1979; Lentz and McAllister 1990; Plimer et al. 1991; Murciego et al. 1997; Serranti et al. 2002; Jiang et al. 2004; Gorelikova et al. (2006); Abdalla et al. 2008; Neiva 2008; Wise and Brown 2011; Pavlova et al.

2015; Lerouge et al. 2017; Nascimento and Souza 2017; Zhang et al. 2017; Guo et al. 2018; Chen et al. 2019; Cheng et al. 2019; Fuchsloch et al. 2019; Hulsbosch and Muchez 2019; Kendall-Langley et al. 2019; Zhao et al. 2019; Zoheir et al. 2019; Mao et al. 2020; Nambaje et al. 2020; Gemrich et al. 2021)

chalcopyrite from mantos (1078–900 ppm; up to 1185 ppm) than in analyzed chalcopyrite from veins (670–535 ppm). In contrast, Ga content is higher in veins (27–14 ppm) than in mantos (1.9–1.5 ppm). Germanium content is similar in chalcopyrite from both mantos and veins (3.2–0.29 ppm).

Cassiterite

Cassiterite from Ayawilca yields moderate enrichment in Fe (12,300–9350 ppm), W (5032–1670 ppm), Si (925–614 ppm), and Ti (416–111 ppm) relative to Mn (12–2.5 ppm) and HFSE (1.8–0.29 ppm Zr, 0.079–0.041 ppm Hf, 0.62–0.040 ppm Nb, 0.021–0.014 ppm Ta) contents. Other elements with values mostly above their respective lower limits of detection include Al (83–56 ppm), V (50–17 ppm), Sb (84–48 ppm), Ni (24–16 ppm), In (89–47 ppm), and Sc (5.0–1.2 ppm).

In the binary Fe + Mn vs. Nb + Ta diagram, the cassiterite data cluster below both the 1:1 (i.e., $2\text{Sn}^{4+} \leftrightarrow (\text{Nb},$

$\text{Ta})^{5+} + (\text{Fe}, \text{Mn})^{3+}$ coupled substitution) and 2:1 (i.e., $3\text{Sn}^{4+} \leftrightarrow 2(\text{Nb}, \text{Ta})^{5+} + (\text{Fe}, \text{Mn})^{2+}$) ratio lines (Fig. 9A) and yield Nb/Ta atomic ratios between 2 and 113 (Fig. 9B). The analyzed cassiterite shows a fairly positive correlation between Ti and Zr at Ti/Zr atomic ratios between 163 and 1361 (Fig. 9C). Scandium also shows fairly positive correlations with Ti (Ti/Sc atomic ratios between 40 and 255; Fig. 9D) and V (V/Sc atomic ratios between 5 and 31; Fig. 9E). Zirconium and Hf yield a positive correlation in the analyzed cassiterite grains at Zr/Hf atomic ratios between 3 and 74 (Fig. 9F).

Rare-earth-element (REE; La to Lu) contents in cassiterite grains from Ayawilca are relatively homogeneous in all analyzed grains ($\sum\text{REE}$ between 4.9 and 0.97 ppm). The highest REE contents correspond to Gd (1.2–0.87 ppm) and La (0.33–0.26 ppm), and the lowest to Tm (0.017–0.013 ppm) and Ho (0.021–0.014 ppm). In chondrite-normalized (CN) spider plots (Fig. S3), studied cassiterite grains show roughly parallel patterns with irregular distribution combining concave and convex tetrads.

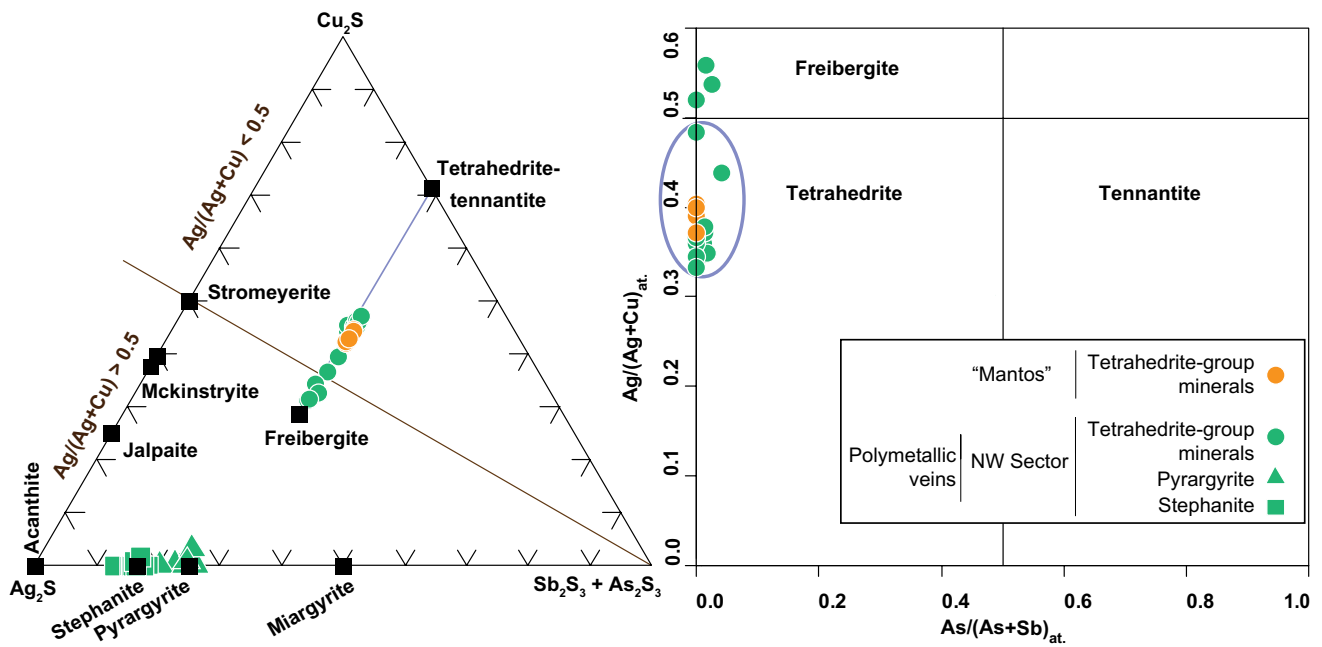


Fig. 10 Plot of the analyzed tetrahedrite-group minerals and Ag–Cu–Sb sulfosalts from the Ayawilca deposit in the Ag_2S vs. $Sb_2S_3 + As_2S_3$ ternary diagram and of the tetrahedrite-group minerals in the $As/(As+Sb)_{at.}$ vs. $Ag/(Ag+Cu)_{at.}$ binary diagram (right) (EPMA data)

Magnetite

Minor and trace elements analyzed in magnetite include Ti (46–4.7 ppm), V (19–2.9 ppm), Mn (1961–1014 ppm), Al (99–21 ppm), Ca (749–218 ppm), Ni (0.76–0.14 ppm), and Cr (2.6–0.40 ppm). The three generations of magnetite from Ayawilca plot within the field of skarn deposits in discrimination diagrams (e.g., Dupuis and Beaudoin 2011; Nadoll 2011; Nadoll et al. 2014; Meng et al. 2017; Fig. S4).

Other mineral phases

Representative EPMA analyses of pyrrhotite, galena, herzenbergite, and tetrahedrite group minerals are provided in Table S2. Pyrrhotite grains in mantos presented Fe contents in the range between 61.4 and 60.6 wt%, and S contents in the range between 40.4 and 37.3 wt%. The Ag content in galena was relatively low (< d.l. to 1.0 wt%). Herzenbergite

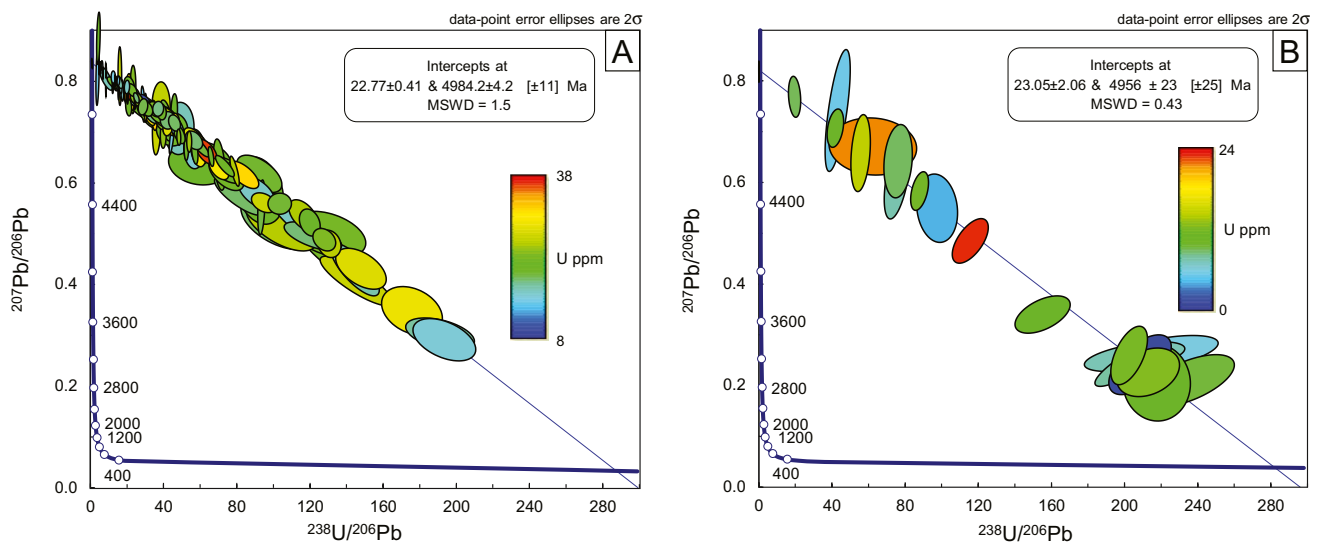


Fig. 11 Tera-Wasserburg (T-W) concordia plots for cassiterite samples from the Ayawilca deposit analyzed at the USGS (A) and ETZH (B)

yields relatively constant Sn (78.9–74.9 wt%) and S (21.3–19.8 wt%) contents.

Analyzed tetrahedrite group minerals yield As/(As + Sb) atomic proportions < 0.03 (Fig. 10) and generally high Ag content both in mantos (between 22.7 and 20.9 wt%) and in veins located in the NW Ayawilca sector (between 32.1 and 19.6 wt%), with Ag/(Ag + Cu) between 0.33 and 0.56. Accordingly, the analyzed tetrahedrite group minerals are classified as tetrahedrite (*var.* Ag-rich tetrahedrite) and freibergite.

Analyzed Ag sulfosalts include pyrargyrite and stephanite from veins at NW Ayawilca (Fig. 10). Pyrargyrite has Ag contents between 56.4 and 62.9 wt%, Sb contents between 17.6 and 22.4 wt%, and S contents between 16.1 and 17.9 wt%. Stephanite yields Ag values between 63.7 and 72.9 wt%, Sb values between 12.1 and 16.6 wt%, and S values between 11.4 and 16.0 wt%.

U–Pb cassiterite geochronology

U–Pb isotopic analyses of cassiterite grains from the Ayawilca deposits are presented in Tables S5–S6 and illustrated in Fig. 11. Although U–Pb concordant data are missing, spot analyses define isochrons in Tera-Wasserburg (T-W; $^{207}\text{Pb}/^{206}\text{Pb}$ vs. $^{238}\text{U}/^{206}\text{Pb}$) diagrams corresponding to mixing lines between the compositions of radiogenic and initial, non-radiogenic Pb in the cassiterite samples. One hundred and twenty spot analyses of cassiterite performed at the USGS laboratory yield a T-W concordia lower intercept date of 22.77 ± 0.41 Ma (2σ ; MSWD = 1.5). Twenty spot analyses carried out at the ETHZ laboratory yield a T-W concordia lower intercept date of 23.05 ± 2.06 Ma (2σ ; MSWD = 0.43; with matrix effect-related uncertainty propagated—see “[Sampling and analytical methods](#)” section for details). The consistency of the two dates (despite different analytical parameters and calibration strategies) supports the notion that the Ayawilca cassiterite crystallized in a single event within the dating uncertainties at ca. 23.1–22.7 Ma and displayed a closed-system behavior with respect to relative U–Pb mobility after formation.

Discussion

Evolution of mineralization conditions

The paragenetic sequences in the polymetallic mantos and veins (Fig. 5) and the chemical compositions of some key minerals are used here to constrain the evolution

of mineralization conditions during formation of the Ayawilca deposit. The earliest mineralization stage in the mantos is identified as a likely distal retrograde magnesian skarn (stage pre-A) that includes locally abundant Mg-siderite + talc + magnetite + chlorite and relict actinolite-tremolite. As mentioned above, the trace element composition of the magnetite is characteristic of skarn. The occurrence of skarn assemblages in the deepest mantos at Ayawilca suggests that the studied replacement bodies were formed in a transition zone between a distal skarn and skarn-free Cordilleran-type carbonate-replacement mineralization styles.

Major mineral assemblages in both the mantos and veins record a change from low- (stage A) to intermediate- (stages B and C) sulfidation states, with the paragenetic sequences being broadly equivalent to those of most Cordilleran-type deposits (Fontboté 2018, 2020). However, unlike other Cordilleran-type deposits in the region that contain cassiterite and stannite in trace amounts (e.g., Baumgartner et al. 2008; Bendezú et al. 2009; Catchpole et al. 2012, 2015; Rottier et al. 2016, 2018), Ayawilca hosts a potentially economic Sn resource that includes fairly abundant cassiterite crystallized during stage pre-A, and minor stannite and rare herzenbergite during stage A (Fig. 5). Minor and trace element compositions of cassiterite from Ayawilca are similar to those from xenothermal and epithermal deposits of the Central Andean tin belt in terms of Nb, Ta, Fe, and Mn, and are depleted in Nb + Ta relative to cassiterite from Sn skarns, greisens, migmatites, granite-hosted, and granite cupolas (Fig. 9A, B; references listed in Fig. 9 caption; “xenothermal” is used here in the sense of Imai et al. 1975, as explained in Gemmrich et al. 2021). The contents of Nb and Ta in cassiterite are strongly dependent on temperature so that cassiterite from low-temperature hydrothermal deposits is relatively depleted in these elements (Lerouge et al. 2017; Zhang et al. 2017). On the other hand, cassiterite from Ayawilca shows Ti/Zr (Fig. 9C) and Ti/Sc (Fig. 9D) ratios similar to xenothermal and epithermal deposits, which are normally higher than for those in cassiterite from Sn skarn, greisen, granite-hosted, and granite cupola mineralizations, probably due to the higher mobility of Zr and Sc relative to Ti in the hydrothermal fluids (Taylor 1979; Plimer et al. 1991; Cheng et al. 2019; Gemmrich et al. 2021). Therefore, trace element geochemistry of cassiterite from Ayawilca accords well with a relatively distal position of the manto mineralization relative to a potential causative intrusion.

Cassiterite from Ayawilca is also similar to cassiterite from the Central Andean tin belt in terms of Hf and Zr contents, with Zr/Hf > 1 and mostly higher than cassiterite in greisen, granite-hosted, and granite cupola mineralizations

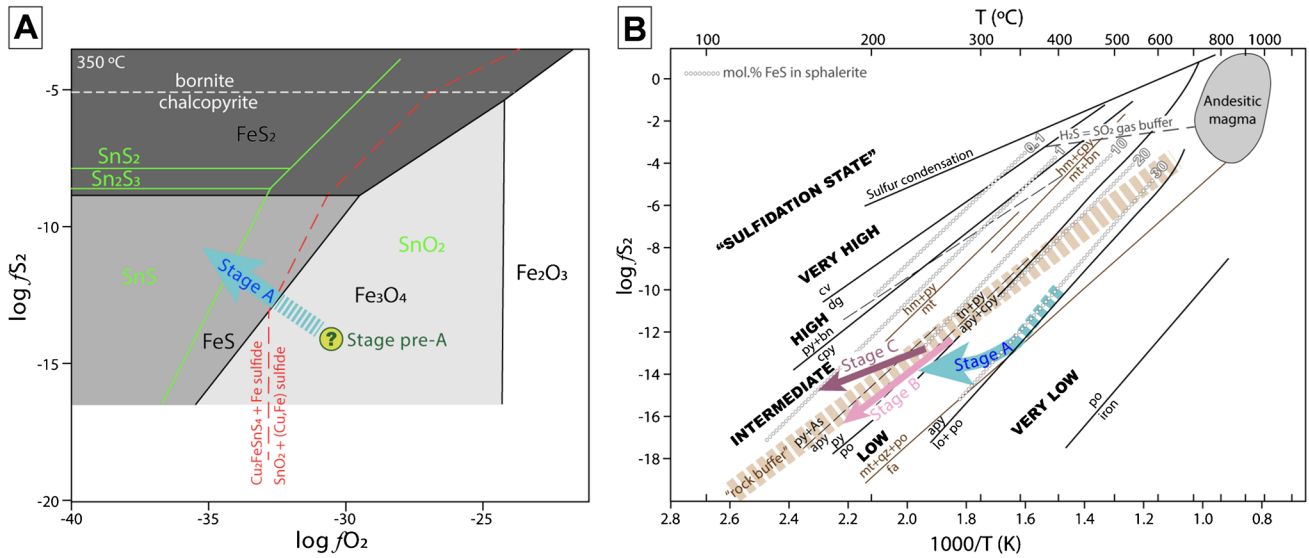


Fig. 12 **A** General fluid path followed by fluids forming stage A in mantos (blue arrow, low sulfidation) in a $\log fS_2$ – $\log fO_2$ isothermal (350 °C) diagram. $\log fS_2$ values inferred from metal-to-sulfur ratios in pyrrhotite (see main text). Position of the blue arrow is only schematic as its origin in the SnO_2 and Fe_3O_4 field does not allow to constrain fS_2 . Field boundaries are after Patterson et al. (1981). **B** General fluid path followed by fluids forming stages A (blue arrow, low sulfidation), B (pink arrow, intermediate sulfidation), and C (purple arrow, intermediate sulfidation) in a $\log fS_2$ – $1000/T$ diagram (modified from Einaudi et al. 2003). Fluid environment is based on sulfide assemblages and the compositions of sulfide and sulfosalt minerals

(see main text), and a preliminary fluid-inclusion study performed by Harlaux (2019). At Ayawilca, the rock-buffer line was probably lower than the one of Giggenbach (1987; shown with a thick, dashed brown line, and based on a fresh andesite) according to the nature of the host rocks, which at Ayawilca include carbonaceous shales and phyllites of the Excelsior Group and carbonates of the Pucará Group. Contours of mol% FeS in sphalerite coexisting with pyrite or pyrrhotite are from Scott and Barnes (1971) and Czamanske (1974). Mineral abbreviations: apy, arsenopyrite; bn, bornite; cpy, chalcopyrite; cv, covellite; dg, digenite; en, enargite; fa, fayalite; fm, famatinite; hm, hematite; lo, löllingite; mt, magnetite; po, pyrrhotite; py, pyrite; qz, quartz

(Fig. 9F). The most likely explanation for this is the preferential mobilization of Zr in B- and F-rich fluids causing fractionation of Zr over Hf in hydrothermal cassiterite (Cheng et al. 2019). However, at Ayawilca, there is a lack of B and F species, which is a significant difference compared with many other Sn(-polymetallic) magmatic-hydrothermal deposits (Pollard et al. 1987; Xiang et al. 2020; Lehmann 2021), including those in the Central Andean tin belt (Kelly and Turneaure 1970; Lehmann et al. 1990, 2000; Cacho et al. 2019; Torres et al. 2019; Harlaux et al. 2020), in which the occurrence of tourmaline + fluorite ± topaz in hydrothermal alteration assemblages is ubiquitous.

The precipitation sequence of cassiterite to stannite to herzenbergite as precipitating Sn phases in the mantos at Ayawilca (Figs. 3K, L and 5) indicates increasingly reducing conditions at relatively low fS_2 in stage pre-A and throughout stage A (Patterson et al. 1981). The occurrence of herzenbergite deserves particular attention. The enhanced solubility of Sn in reduced media (Patterson et al. 1981; Barsukov et al. 1987; Heinrich 1990; Linnen et al. 1995; Lehmann 2021) renders crystallization and preservation of herzenbergite unlikely, hence the global scarcity of localities in which it has been documented. The crystallization of herzenbergite

is promoted by exceptionally low fO_2 ($\sim 10^{-40}$ – 10^{-35} atm) at relatively low fS_2 —normally in equilibrium with pyrrhotite—over a wide range of temperature (~ 200 – 500 °C) and pH (2–10) conditions (Patterson et al. 1981; Smeds 1993 and references therein). Intense chemical buffering of hydrothermal fluids during their interaction with the Excelsior carbonaceous phyllites probably resulted in a significant fO_2 drop to values low enough to stabilize herzenbergite after initial crystallization of cassiterite in the slightly more oxidized sulfur field (Fig. 12A).

A preliminary fluid inclusion study of stage A quartz postdating pyrrhotite yielded homogenization temperatures in the range between 341 and 265 °C (average of 298 ± 22 °C) and salinities between 2.4 and 9.1 wt% NaCl equiv. (Harlaux 2019). If we assume that cassiterite crystallized at higher temperatures than stage A quartz (Fig. 5), a plausible stage A quartz-pyrrhotite and minimum cassiterite crystallization temperatures would be around 350 °C. At 350 °C, atomic metal to sulfur ratios in analyzed pyrrhotite yield $\log fS_2$ in the approximate range between –13 and –10 atm (Toulmin and Barton 1964). According to this fS_2 range, herzenbergite would have formed at $\log fO_2$ in the approximate range between –30 and –35 atm, which likely

represents the minimum fO_2 value reached by hydrothermal fluids at Ayawilca (Fig. 12A). Sealing of the walls of mineralized structures by quartz along with waning wall-rock buffering capacity favored a progression from low sulfidation (stage A) to higher sulfidation (stages B and C) states as the system cooled (see Baumgartner et al. 2008 and Rottier et al. 2018).

Sphalerite from Ayawilca mantos and veins records a pronounced decrease in the Fe content from the early (stage A) to late (stage C; Fig. 5) generations. The compositions of sphalerite crystallized during stage A in mantos (first generation 30 to 18 mol% FeS, avg. 22 mol% FeS; second-generation 32 to 10 mol% FeS, avg. 22 mol% FeS) and veins at NW Ayawilca (33 to 9 mol% FeS, avg. 19 mol% FeS) and NE Ayawilca (21 to 18 mol% FeS, avg. 19 mol% FeS) accord well with general crystallization in equilibrium with pyrrhotite and beyond the pyrite stability field at about > 21 mol% FeS (Scott and Barnes 1971). FeS values in the range between 19 and 21 mol% suggest co-crystallization in equilibrium with both pyrite and pyrrhotite, and FeS < 19 mol% values suggest crystallization in equilibrium with pyrite and beyond the pyrrhotite stability field. According to these observations, sphalerite records a progressive shift from low- to intermediate-sulfidation states during the transition from stage A to stage B at Ayawilca. At $\log fS_2$ of -10 atm or lower, sphalerite with 33 mol% FeS would have crystallized at a maximum temperature of ~ 380 °C, and sphalerite with 21 mol% FeS at a maximum temperature of 318 °C (Scott and Barnes 1971). Stage C sphalerite from the mantos (7 to 3 mol% FeS, avg. 4 mol% FeS) and veins (11 to 1 mol% FeS, avg. 8 mol% FeS) yields compositions that indicate crystallization in equilibrium with pyrite and beyond the pyrrhotite stability field.

The composition of co-crystallized sphalerite and stannite (stage A; Fig. 5) yields formation temperatures in the range between 300 and 250 °C according to the Nakamura and Shima (1982) geothermometer. Finally, the composition of tetrahedrite group minerals that crystallized during stage C (Fig. 5) yields crystallization temperatures in the range between 200 and 170 °C for analyzed grains from the mantos and between 300 and 170 °C for analyzed grains from NW Ayawilca veins according to the Sack et al. (2003) geothermometer. However, temperatures < 200 °C are probably unrealistically low for main tetrahedrite crystallization if they are compared with Ti-in-quartz thermobarometry and microthermometric data measured in stage C inclusion fluids in other Cordilleran-type polymetallic deposits (e.g., Catchpole et al. 2015; Rottier et al. 2018, 2021). Possible pathways of fluid evolution leading to the deposition of the sulfides and sulfosalts in the Ayawilca polymetallic mantos and veins are shown on a $\log fS_2$ vs. $1000/T$ diagram in Fig. 12B.

Mineralogical expression and distribution of indium

In the Ayawilca deposit, In is found within the crystal lattice of some major minerals, and no independent In minerals (e.g., roquesite) were found. This situation is typical of polymetallic deposits in which Zn is a major component and sphalerite fairly abundant (Cook et al. 2011b). According to our dataset, the main In-bearing minerals at Ayawilca are sphalerite (986–16 ppm, up to 1.7 wt%), stannite (1168–809 ppm, up to 1908 ppm), and chalcopyrite (910–537 ppm, up to 1185 ppm).

Sphalerite is volumetrically the most abundant sulfide mineral in both the polymetallic mantos and veins at Ayawilca and therefore represents the main In host at the deposit scale. Effective partitioning of In into sphalerite has been extensively documented (Cook et al. 2009, 2011a, 2011b; Sahlström et al. 2017; Bauer et al. 2019; Carvalho et al. 2018; Torró et al. 2019a, 2019b; Benites et al. 2021). Relatively high In content in Fe-rich sphalerite (avg. 2620 ppm) was reported by Rottier et al. (2016) in the neighboring Cerro de Pasco deposit (Fig. 1). The strong positive correlation between the atomic contents of In and Cu in the studied sphalerite grains that are partly distributed along the 1:1 ratio line (Fig. 7E) points to a $Cu^+ + In^{3+} \leftrightarrow 2 Zn^{2+}$ coupled substitution (Patrick et al. 1993; Schwarz-Schampera and Herzig 2002; Cook et al. 2011a, 2011b; 2012; Torró et al. 2019a, b) in the frame of a sphalerite–roquesite solid solution (Oen et al. 1980; Parasyuk et al. 2003; Schorr and Wagner 2005). However, the totality of the analyzed sphalerite from the NE and NW Ayawilca vein systems and part of the analyzed sphalerite from the mantos plot above the Cu:In = 1:1 correlation line, thus denoting higher Cu at a given In content. A similar situation is noticed by others (e.g., Xu et al. 2020) and points to the existence of further coupled substitutions involving Cu. The marked positive correlation between Cu + Ag and Ga + Ge + In + Sn in sphalerite, whose compositions are massively distributed along the 1:1 ratio line (Fig. 7F), supports a $(Sn, Ge)^{4+} + (Ga, In)^{3+} + (Cu + Ag)^+ \leftrightarrow 4 Zn^{2+}$ coupled substitution (Cook et al. 2009). Therefore, besides Cu, elements such as Ag and Sn also played an important role in the incorporation of In into the sphalerite crystal lattice.

In contrast to sphalerite, the incorporation of In into the stannite crystal lattice is poorly understood. Torró et al. (2019a) suggested, after the study of In-rich stannite grains from the Huari Huari district in the Central Andean tin belt, an $In^{3+} \leftrightarrow (Cu^+ + \frac{1}{2} Sn^{4+})$ coupled substitution. However, no clear correlation trends that would involve these elements were observed in stannite from Ayawilca. The incorporation of In into the crystal lattice of stannite in the frame of a hypothetical stannite–(In-rich) sphalerite solid solution within the $(Zn, Fe)S-Cu_2FeSnS_4-CuInS_2$ pseudoternary

system described by Oen et al. (1980) is likewise implausible according to the lack of correlation between Zn and In within this mineral at Ayawilca (Fig. 8D).

As observed in stannite, In does not show clear correlation trends with the other analyzed elements in chalcopyrite from Ayawilca. Due to covalent bonding, a substitution mechanism based on element correlation trends and electro-neutrality cannot be straightforwardly deduced for chalcopyrite (George et al. 2018). Wittmann (1974) suggested that significant In could be hosted in chalcopyrite (mostly in the Fe site) because it is isostructural with roquesite. The reader is referred to Belissont et al. (2019) and Reich et al. (2020) for previously proposed coupled substitutions in chalcopyrite that involve In.

Although cassiterite may host important In contents (e.g., up to 485 ppm in granites and granite cupolas from the Nghe An deposit, Vietnam, Pavlova et al. 2015; up to 1430 ppm in epithermal deposits from the Central Andean tin belt, Gemmrich et al. 2021), the contents of this *high-tech* metal recorded in cassiterite from Ayawilca are relatively low (89–47 ppm, up to 98 ppm). Lerouge et al. (2019) stated that sulfides (i.e., sphalerite and stannite) with high In contents were often related to In-poor cassiterite, and attributed this fact to a high sulfide/cassiterite partition coefficients. However, as cassiterite crystallized earlier than In-bearing sulfides at Ayawilca (Fig. 5), this hypothesis may not be relevant and may just reflect low concentrations of In in the mineralizing fluids during the crystallization of cassiterite (see Plimer et al. 1991; Gemmrich et al. 2021).

The detailed study of the mineralogy and textures in the Ayawilca deposit poses some temporal constraints on the distribution of In across the paragenetic sequences. The highest contents of In are associated with stage A second-generation sphalerite from the mantos and with stage A sphalerite from the NE Ayawilca veins (a single generation was found there; Figs. 5, 6F). Therefore, high In content in sphalerite from Ayawilca typically correlates with high Fe content, but the opposite is not necessarily true. For example, stage A first-generation sphalerite in the mantos is Fe-rich (as typical of low-sulfidation assemblages) but In poor (Fig. 6A, F). Stage C sphalerite in both the veins from NW Ayawilca and mantos, which formed from late intermediate-sulfidation state fluids (Fig. 5), is systematically In poor (Fig. 6F). Accordingly, low-sulfidation assemblages that contain abundant sphalerite, chalcopyrite, and stannite are the most prospective for In in Cordilleran-type deposits, especially in those with large volumes of low-sulfidation assemblages, as at Ayawilca. Torr o et al. (2019a) identified similar temporal trends in the distribution of In in sphalerite from the xenothermal Huari Huari deposit, including In enrichment (up to 9 wt% In) in sphalerite that crystallized during early stages in a low-sulfidation paragenesis in equilibrium with stannite and chalcopyrite. These authors

proposed that the co-crystallization of In-rich sphalerite with stannite and chalcopyrite and the strong positive correlation between In and Cu in sphalerite were indicative of a high Cu activity in the hydrothermal fluids, which enabled the incorporation of In into the sphalerite crystal lattice through the substitution mechanisms discussed above.

Regarding the spatial distribution of In content across the deposit, the highest In values in sphalerite from Ayawilca are found at relatively deep levels (e.g., up to 1.7 wt% In at 347.50 m). However, no steady enrichment of In in sphalerite with depth has been noted, and some high In values have been detected in relatively shallow locations as well (e.g., up to 3778 ppm In at 240.10 m; stage A mineralization in mantos). The morphology of the mineralization did not apparently exert any control on In enrichment either: stage A second-generation sphalerite from mantos and sphalerite from the NE Ayawilca veins yield similar In contents (Fig. 6).

The Ayawilca deposit within the metallogenic evolution of the central Andes

Direct U–Pb dating of cassiterite at ca. 23.1–22.7 Ma constrains the age of the Ayawilca deposit as earliest Miocene, suggesting assignment of the Ayawilca deposit to the Miocene polymetallic belt in central Peru. However, it is older than most deposits in this belt, which are mostly mid-Miocene or younger (ca. 15–5 Ma—e.g., Domo de Yauli, Morococha, Cerro de Pasco, Colquijirca, Antamina; Beuchat et al. 2004; Baumgartner et al. 2008; Bendez u and Fontbot e 2009; Longo et al. 2010; Catchpole et al. 2015; Rottier et al. 2018; Mrozek et al. 2020). Ayawilca appears to be only slightly younger than the late Oligocene Uchucchacua polymetallic deposit (ca. 24.5 Ma; Bissig et al. 2008). The obtained age for the cassiterite of Ayawilca supports the conclusion of the latter authors that potential for polymetallic deposits in central Peru is greater near intrusive rocks of mid to late Miocene age except for an easterly striking broad strip at ~10°40′–10°50′S where the late Eocene and Oligocene Uchucchacua (ca. 24.5 Ma), Milpo (now also called El Porvenir–Atachocha (ca. 29.5 Ma)), and Quicay (ca. 37.5 Ma) deposits occur (Bissig et al. 2008). The early Miocene Ayawilca deposit located at 10°43′S occurs in this very transect. Bissig et al. (2008) pointed out that subduction geometry alone cannot account for the observed distribution of mineralization and that specific upper-plate features in this transect should also have exerted a metallogenic control. North of 8°S and still inside the Miocene–early Pliocene porphyry belt of the central Andes (Sillitoe and Perell o 2005), mineralization events bracketed at ca. 22–20 Ma occur in the Cajamarca mining district in northern Peru, including the Michiquillay and Aurora Patricia porphyry Cu–Mo deposits (Laughlin et al. 1968; Noble et al. 2004; Davies 2002;

Davies and Williams 2005; Carlotto et al. 2009; Marinov 2011), which are located ~420 km north of Ayawilca. The Malvas and Huinac porphyry districts in the Cordillera Negra (Noble et al. 2004), which are located ~150 km northwest of Ayawilca, also fall into this age range.

The discovery of the Ayawilca deposit has important implications for exploration in the central Andes as it hosts a potentially economic Sn resource located ~850 km northwest of the northern tip of the Central Andean tin belt (Fig. 1). The obtained U–Pb cassiterite age for Ayawilca overlaps, within analytical error, the age of Sn mineralization in the northern portion of the Central Andean tin belt, including the world-class San Rafael deposit and Santo Domingo and Palca occurrences in southeastern Peru, and the Viloco, Huanuni, and Llallagua deposits in Bolivia (radiometric dates summarized in Gemrich et al. 2021). In contrast to the Miocene–early Pliocene porphyry belt, in which causative intrusions have “regular” calc-alkaline affinities and belong to the I-type, magnetite series of Ishihara (1981), the causative intrusions in the Central Andean tin belt belong to the S-type, ilmenite series (Sillitoe and Perelló 2005; Fontboté 2018; Lehmann 2021). At Ayawilca, the causative intrusion remains concealed, and therefore, its petrogenetic nature is unknown. Although a relatively reduced magma is required to exsolve tin into comagmatic hydrothermal fluids (tin behaves as an incompatible element in the divalent state; Lehmann 2021), peraluminous, ilmenite-series intrusive rocks of Cenozoic age are apparently absent in the study area and everywhere north of 14°S (i.e., north of the San Rafael tin district; Harlaux et al. 2020 and references therein). The highly reduced nature of the Excelsior carbonaceous phyllites beneath the deposit would have favored effective transport of Sn (Heinrich 1990; Xiang et al. 2020; Lehmann 2021). As a preliminary hypothesis, we surmise that due to the absence of the Mitu Group red beds at Ayawilca (Figs. 1 and 2), in contrast to several other Cordilleran-type polymetallic deposits in the region (e.g., Morococha and Colquijirca), rock buffering of the hydrothermal fluids was particularly intense, facilitating Sn²⁺ transport and an economic accumulation of Sn as cassiterite. However, it should be noted that at Cerro de Pasco, where the available evidence indicates that the Excelsior phyllites strongly buffered the hydrothermal fluid, only minor cassiterite and stannite occur (Baumgartner et al. 2008; Rottier et al. 2016, 2018) and that the tin endowment at Ayawilca is several orders of magnitude higher.

Conclusions

The Ayawilca deposit is one of the most significant recent base-metal discoveries in the central Andes and one of the largest undeveloped In resources worldwide. The

mineralization at Ayawilca occurs as 10- to 70-m-thick mantos and subordinate steeply dipping veins. The Sn-dominant resource is hosted by massive pyrrhotite replacement bodies at the base of the Triassic to Early Jurassic carbonate rocks of the Pucará Group, close to and along their contact with underlying Devonian weakly metamorphosed, organic-rich shaly rocks of the Excelsior Group. Zinc mineralization occurs predominantly as Fe-rich sphalerite mantos and veins hosted in rocks of the Pucará Group and, subordinately, in Cretaceous sandstones-siltstones of the Goyllarisquizga Group.

The mineralization at Ayawilca includes relicts of a distal retrograde magnesian skarn composed of Mg-siderite + talc + magnetite + chlorite ± actinolite-tremolite, which along with cassiterite formed prior to the main sulfide mineralization stages (stage pre-A). The volumetrically most important mineralization comprises a low-sulfidation assemblage (stage A) composed of quartz, pyrrhotite, and arsenopyrite, and subsequent chalcopyrite, Fe-rich sphalerite (up to 33 mol% FeS), stannite, and herzenbergite. Pre-A and A stage mineral assemblages are overprinted by an intermediate-sulfidation assemblage (stage B) composed of pyrite, marcasite, and intermediate product. Mineral assemblages from pre-A, A, and B stages are overprinted by a further intermediate-sulfidation assemblage (stage C) composed of sphalerite (up to 11 mol% FeS), galena, native bismuth, Cu–Pb–Ag sulfosalts, chalcopyrite, siderite, Mn–Fe carbonates, kaolinite, dickite, and sericite.

The mineral paragenesis at Ayawilca suggests emplacement of the manto mineralization as a transition between retrograde skarn and Cordilleran-type carbonate-replacement mineralization. A preliminary fluid-inclusion study (Harlaux 2019) points to crystallization of quartz-pyrrhotite in stage A at temperatures as high as ~350 °C. The occurrence of herzenbergite [SnS] after cassiterite and stannite suggests increasingly reducing conditions from initial crystallization of cassiterite under slightly more oxidizing conditions in stage pre-A to extremely low log f_{O_2} values between ~ –30 and –35 atm during the crystallization of herzenbergite in stage A, assuming a temperature of 350 °C and a log f_{S_2} of –13 to –10 atm. The composition of Fe-rich sphalerite and stannite that crystallized in equilibrium during stage A suggests that crystallization occurred at temperatures around 300–250 °C.

A significant decrease in f_{O_2} could have been effectively achieved through intense buffering of hydrothermal fluids by the carbonaceous Excelsior Group during initial stages of the sulfide mineralization. Cooling, progressive sealing of vein walls by quartz, and decreasing redox potential of the host rocks drove the evolution from low-sulfidation (stage A) to intermediate-sulfidation (stages B and C) states of the mineralizing fluids. The reducing

character of the carbonaceous Excelsior Group favored a low oxidation state, thus enhancing Sn mobility.

The main In hosts at Ayawilca are stage A sphalerite, stannite (IQR 1168–809 ppm, up to 1908 ppm), and stages A and C chalcopyrite (IQR 910–537 ppm, up to 1185 ppm). The highest In contents are found in second-generation sphalerite crystallized during stage A (IQR 1299–227 ppm, up to 1.7 wt%). Indium was likely incorporated into the crystal lattice of sphalerite via $\text{Cu}^+ + \text{In}^{3+} \leftrightarrow 2 \text{Zn}^{2+}$ and $(\text{Sn}, \text{Ge})^{4+} + (\text{Ga}, \text{In})^{3+} + (\text{Cu} + \text{Ag})^+ \leftrightarrow 4 \text{Zn}^{2+}$ coupled substitutions. The substitution mechanisms of In in the stannite and chalcopyrite crystal lattices remain unclear.

With the obtained LA-ICP-MS U–Pb cassiterite dates (22.77 ± 0.41 and 23.05 ± 2.06 Ma, early Miocene), Ayawilca is older than most deposits in the NNW-SSE-trending polymetallic belt of central Peru, which are mostly mid-Miocene or younger. Within this belt, Ayawilca and the Oligocene Uchucchacua and Milpo-Atacocha deposits appear to be part of an easterly striking broad strip at $\sim 10^\circ 40' - 10^\circ 50' \text{S}$ in which slightly older deposits occur. Unlike other deposits in the polymetallic belt of central Peru, in which only minor Sn-bearing minerals have been described, Ayawilca hosts a potentially economic Sn resource, thereby expanding the prospective region for this metal for ~ 850 km northwest from the northernmost tip of the Central Andean tin belt.

Supplementary Information The online version contains supplementary material available at <https://doi.org/10.1007/s00126-021-01066-z>.

Acknowledgements This study was economically supported by the Peruvian CONCYTEC-FONDECYT-World Bank project 107-2018-FONDECYT-BM-IADT-AV and the Mexican research program CONACYT-Ciencia Básica (A1-S-14574). We thank the staff of Tinka Resources Ltd., particularly to Jorge Gamarra, for help and hospitality during the sampling program. We appreciate the technical support by Xavier Llovet (CCiT-UB) and Carlos Ortega Obregón (LEI-UNAM) during acquisition of EPMA data, and by Pete Tollan (ETH) during acquisition of LA-ICP-MS data. We are grateful to Richard Sil-litoe, Andreas Dietrich, Graham Carman (president and CEO of Tinka Resources), and Editor-in-Chief Bernd Lehmann for their constructive comments which significantly improved the manuscript. Any use of trade, firm, or product names is for descriptive purposes only and does not imply endorsement by the U.S. Government.

References

- Abdalla HM, Matsueda H, Obeid MA, Takahashi R (2008) Chemistry of cassiterite in rare metal granitoids and the associated rocks in the Eastern Desert. *Egypt J Miner Petrol Sci* 103:318–326
- Andersen JC, Stickland RJ, Rollinson GK, Shail RK (2016) Indium mineralisation in SW England: host parageneses and mineralogical relations. *Ore Geol Rev* 78:213–238
- Barsukov VL, Durasova NA, Kovalenko NI, Ryabchikov ID, Ryzenko BN (1987) Oxygen fugacity and tin behaviour in melts and fluids. *Geol Zbornik-Geot Carpatia* 38:723–733
- Bauer ME, Burisch M, Ostendorf J, Krause J, Frenzel M, Seifert T, Gutzmer J (2019) Trace element geochemistry of sphalerite in contrasting hydrothermal fluid systems of the Freiberg district, Germany: insights from LA-ICP-MS analysis, near-infrared light microthermometry of sphalerite-hosted fluid inclusions, and sulfur isotope geochemistry. *Miner Deposita* 54:237–262
- Baumgartner R, Fontboté L, Vennemann T (2008) Mineral zoning and geochemistry of epithermal polymetallic Zn-Pb-Ag-Cu-Bi mineralization at Cerro de Pasco, Peru. *Econ Geol* 103:493–537
- Baumgartner R, Fontboté L, Spikings R, Ovtcharova M, Schaltegger U, Schneider J, Page L, Gutjahr M (2009) Bracketing the age of magmatic-hydrothermal activity at the Cerro de Pasco epithermal polymetallic deposit, Central Peru: a U-Pb and $^{40}\text{Ar}/^{39}\text{Ar}$ study. *Econ Geol* 104:479–504
- Belissant R, Munoz M, Boiron M, Luais B, Mathon O (2019) Germanium crystal chemistry in Cu bearing sulfides from micro-XRF mapping and micro-XANES spectrometry. *Minerals* 9:227
- Benavides-Cáceres V (1999) Orogenic evolution of the Peruvian Andes: the Andean Cycle. *Soc Econ Geol Spec Pub* 7:61–107
- Bendézú R, Fontboté L (2009) Cordilleran epithermal Cu-Zn-Pb-(Au-Ag) mineralization in the Colquijirca district, Central Peru: deposit-scale mineralogical patterns. *Econ Geol* 104:905–944
- Bendézú R, Page L, Spikings R, Pecsckay Z, Fontboté L (2008) New $^{40}\text{Ar}/^{39}\text{Ar}$ alunite ages from the Colquijirca district, Peru: evidence of a long period of magmatic SO_2 degassing during formation of epithermal Au-Ag and Cordilleran polymetallic ores. *Miner Deposita* 43:777–789
- Benites D, Torró L, Vallance J, Laurent O, Valverde PE, Kouzmanov K, Chelle-Michou C, Fontboté L (2021) Distribution of indium, germanium, gallium and other minor and trace elements in polymetallic ores from a porphyry system: the Morococha District, Peru. *Ore Geol Rev* 136, 104236
- Beuchat S, Moritz R, Pettke T (2004) Fluid evolution in the W-Cu-Zn-Pb San Cristobal vein, Peru: fluid inclusion and stable isotope evidence. *Chem Geol* 210:201–224
- Bissig T, Ullrich TD, Tosdal RM, Friedman R, Ebert S (2008) The time-space distribution of Eocene to Miocene magmatism in the central Peruvian polymetallic province and its metallogenic implications. *J S Am Earth Sci* 26:16–35
- Cacho A, Melgarejo JC, Camprubí A, Torró L, Castillo-Oliver M, Torres B, Artiaga D, Tauler E, Martínez A, Campeny M, Alfonso P, Arce-Burgoa OR (2019) Mineralogy and distribution of critical elements in the Sn-W-Pb-Ag-Zn Huanuni Deposit. *Bolivia Minerals* 9:753
- Cardona A, Cordani UG, Ruiz J, Valencia VA, Armstrong R, Chew D, Nutman A, Sanchez AW (2009) U-Pb zircon geochronology and Nd isotopic signatures of the pre-Mesozoic metamorphic basement of the Eastern Peruvian Andes: growth and provenance of a late Neoproterozoic to Carboniferous accretionary orogen on the northwest margin of Gondwana. *J Geol* 117:285–305
- Carlotto V, Quispe J, Acosta H et al (2009) Geotectonic domains as tool for metallogenetic mapping in Peru. *Bol Soc Geol Perú* 103:1–89
- Carvalho JRS, Relvas JMRS, Pinto AMM, Frenzel M, Krause J, Gutzmer J, Reis T (2018) Indium and selenium distribution in the Neves-Corvo deposit, Iberian Pyrite Belt, Portugal. *Mineral Mag* 82:S5–S41
- Catchpole H, Kouzmanov K, Fontboté L (2012) Copper-excess stannoidite and tennantite-tetrahedrite as proxies for hydrothermal fluid evolution in a zoned Cordilleran base metal district, Morococha, central Peru. *Can Mineral* 50:719–743
- Catchpole H, Kouzmanov K, Putlitz B, Seo J, Fontboté L (2015) Zoned base metal mineralization in a porphyry system: origin and evolution of mineralizing fluids in the Morococha District, Peru. *Econ Geol* 110:39–71

- Chen LL, Ni P, Dai BZ, Li WS, Chi Z, Pan JY (2019) The genetic association between quartz vein- and greisen-type mineralization at the Maoping W-Sn Deposit, Southern Jiangxi, China: insights from zircon and cassiterite U–Pb ages and cassiterite trace element composition. *Minerals* 9:411
- Cheng Y, Spandler C, Kemp A, Mao J, Rusk B, Hu Y, Blake K (2019) Controls on cassiterite (SnO₂) crystallization: evidence from cathodoluminescence, trace-element chemistry, and geochronology at the Gejiu tin district. *Am Mineral* 104:118–129
- Chew DM, Schaltegger U, Košler J, Whitehouse MJ, Gutjahr M, Spikings RA, Mišković A (2007) U–Pb geochronologic evidence for the evolution of the Gondwanan margin of the north-central Andes. *Geol Soc Am Bull* 119:697–711
- Chew DM, Pedemonte G, Corbett E (2016) Proto-Andean evolution of the Eastern Cordillera of Peru. *Gondwana Res* 35:59–78
- Cook NJ, Ciobanu CL, Pring A, Skinner W, Shimizu M, Danyushevsky L, Saini-Eidukat B, Melcher F (2009) Trace and minor elements in sphalerite: a LA-ICP-MS study. *Geochim Cosmochim Acta* 73:4761–4791
- Cook NJ, Ciobanu CL, Williams T (2011) The mineralogy and mineral chemistry of indium in sulphide deposits and implications for mineral processing. *Hydrometallurgy* 108:226–228
- Cook NJ, Sundblad K, Valkama M, Nygård R, Ciobanu CL, Danyushevsky L (2011) Indium mineralisation in A-type granites in southeastern Finland: insights into mineralogy and partitioning between coexisting minerals. *Chem Geol* 284:62–73
- Cook NJ, Ciobanu CL, Brugger J, Etschmann B, Howard DL, de Jonge MD, Ryan C, Paterson D (2012) Determination of the oxidation state of Cu in substituted Cu–In–Fe-bearing sphalerite via μ XANES spectroscopy. *Am Mineral* 97:476–479
- Czamaske GK (1974) The FeS content of sphalerite along the chalcopyrite–pyrite–bornite sulfur fugacity buffer. *Econ Geol* 69:1328–1334
- Dalmayrac B, Laubacher G, Marocco R (1988) Caracteres generales de la evolución geológica de los Andes Peruanos. *INGEMMET. Boletín, Serie D Estudios Regionales* 12, 326 p.
- Davies RC (2002) Tectonic, magmatic and metallogenic evolution of the Cajamarca mining district, Northern Peru. Unpublished PhD thesis, James Cook University, Townsville, Australia, 323 p
- Davies RC, Williams PJ (2005) The Galeno and Michiquillay porphyry Cu–Au–Mo deposits: geological descriptions and comparison of Miocene porphyry systems in the Cajamarca district, northern Peru. *Miner Deposita* 40:598–616
- Dupuis C, Beaudoin G (2011) Discriminant diagrams for iron oxide trace element fingerprinting of mineral deposit types. *Miner Deposita* 46:319–335
- Einaudi MT, Hedenquist JW, Inan E (2003) Sulfidation state of hydrothermal fluids: the porphyry–epithermal transition and beyond. *Soc Economic Geol Geoch Soc Spec Publ* 10:285–313
- Eude A, Roddaz M, Brichau S, Brusset S, Baby P, Calderon Y, Soula JC (2015) Control of timing of exhumation and deformation in the northern Peruvian Eastern Andean Wedge (5–8 S) as inferred from low temperature thermochronology and balanced cross section. *Tectonics* 34:715–730
- Fontboté L (2018) Ore deposits of the Central Andes. *Elements* 14:257–261
- Fontboté L (2020) Systematic trends in the evolution of porphyry-related Zn–Pb–(Ag) deposits. Abstracts of the Swiss Geoscience Meeting, Zurich, p. 40–41
- Frenzel M, Ketris MP, Gutzmer J (2014) On the geological availability of germanium. *Miner Deposita* 49:471–486
- Frenzel M, Hirsch T, Gutzmer J (2016) Gallium, germanium, indium, and other trace and minor elements in sphalerite as a function of deposit type – a meta-analysis. *Ore Geol Rev* 76:52–78
- Frenzel M, Ketris MP, Seifert T, Gutzmer J (2016b) On the current and future availability of gallium. *Resour Policy* 47:38–50
- Fuchsloch W, Nex P, Kinnaird J (2019) The geochemical evolution of Nb–Ta–Sn oxides from pegmatites of the Cape Cross–Uis pegmatite belt, Namibia. *Mineral Mag* 83:1–56
- Gamarra J, Fernández-Baca A, Carman G, Giraldo L, Chaiña R, Carrillo H (2019) New exploration ideas for the Ayawilca zinc–silver–indium–tin property, Central Peru. Proceedings of proEXPLOR, Lima 2019. <http://www.proexplo.com/2019/docs/programa/L08.pdf>. Accessed 7 September 2020
- Gaspar OC (2002) Mineralogy and sulfide mineral chemistry of the Neves Corvo ores, Portugal: insight into their genesis. *Can Mineral* 40:611–636
- Gemmrich L, Torró L, Melgarejo JC, Laurent O, Vallance J, Chelle-Michou C, Sempere TPA (2021) Trace element composition and U–Pb ages of cassiterite from the Bolivian tin belt. *Miner Deposita*, in Press. <https://doi.org/10.1007/s00126-020-01030-3>
- George LL, Cook NJ, Ciobanu CL (2016) Partitioning of trace elements in co-crystallized sphalerite–galena–chalcopyrite hydrothermal ores. *Ore Geol Rev* 77:97–116
- George LL, Cook NJ, Crowe BB, Ciobanu CL (2018) Trace elements in hydrothermal chalcopyrite. *Mineral Mag* 82:59–88
- Giggenbach WF (1987) Redox processes governing the chemistry of fumarolic gas discharges from White Island, New Zealand. *Appl Geochem* 2:143–161
- Gorelikova NV, Tolosana-Delgado R, Pawlowsky-Glahn V, Khanchuk A, Gonevchuk V (2006) Discriminating geodynamical regimes of tin ore formation using trace element composition of cassiterite: the Sikhote’Alin case (Far Eastern Russia). *Geol Soc Lond Spec Publ* 264:43–57
- Graeser S (1969) Minor elements in sphalerite and galena from Binnatal. *Contrib Mineral Petrol* 24:156–163
- Guo J, Zhang RQ, Sun WD, Ling MX, Hu YB, Wu K, Zhang LC (2018) Genesis of tin-dominant polymetallic deposits in the Dachang district, South China: insights from cassiterite U–Pb ages and trace element compositions. *Ore Geol Rev* 95:863–879
- Harlaux M (2019) Fluid inclusion study of the early pyrrhotite mineralization stage from the Ayawilca Zn–In–Ag–Sn deposit. Tinka Resources, internal unpublished report, Peru, p 22
- Harlaux M, Kouzmanov K, Gialli S, Laurent O, Rielli A, Dini A, Chauvet A, Menzies A, Kalinaj M, Fontboté L (2020) Tourmaline as a tracer of late-magmatic to hydrothermal fluid evolution: the world-class San Rafael tin (–copper) deposit, Peru. *Econ Geol* 115:1665–1697
- Heinrich CA (1990) The chemistry of hydrothermal tin(–tungsten) ore deposition. *Econ Geol* 85:457–481
- Imai H, Lee MS, Iida K, Fujiki Y, Takenouchi S (1975) Geologic structure and mineralization of xenothermal vein-type deposits in Japan. *Econ Geol* 70:647–676
- Hulsbosch N, Muchez P (2019) Tracing fluid saturation during pegmatite differentiation by studying the fluid inclusion evolution and multiphase cassiterite mineralisation of the Gatumba pegmatite dyke system (NW Rwanda). *Lithos* 354–355:105285
- Ishihara S (1981) The granitoid series and mineralization. In: Skinner BJ (ed) *Economic Geology 75th Anniversary Volume*, pp 458–484
- Jaillard E, Arnaud-Vanneau A (1993) The Cenomanian–Turonian transition on the Peruvian margin. *Cretac Res* 14:585–605
- Jenks WF (1951) Triassic to Tertiary stratigraphy near Cerro de Pasco, Peru. *Geol Soc Am Bull* 62:202–220
- Jiang SY, Yu JM, Lu JJ (2004) Trace and rare-earth element geochemistry in tourmaline and cassiterite from the Yunlong tin deposit, Yunnan, China: implication for migmatitic–hydrothermal fluid evolution and ore genesis. *Chem Geol* 209:193–213
- Jiménez-Franco A, Alfonso P, Canet C, Trujillo J (2018) Mineral chemistry of In-bearing minerals in the Santa Fe mining district, Bolivia. *Andean Geol* 45:410–432

- Kelly WC, Turneure FS (1970) Mineralogy, paragenesis and geothermometry of the tin and tungsten deposits of the Eastern Andes, Bolivia. *Econ Geol* 65:609–680
- Kendall-Langley L, Kemp A, Grigson J, Hammerli J (2019) U-Pb and reconnaissance Lu-Hf isotope analysis of cassiterite and columbite group minerals from Archean Li-Cs-Ta type pegmatites of Western Australia. *Lithos* 352–353:105231
- Laughlin AW, Damon PE, Watson BN (1968) Potassium argon dates from Toquepala and Michiquillay, Peru. *Econ Geol* 63:166–168
- Lehmann B (2021) Formation of tin ore deposits: a reassessment. *Lithos* 105756. <https://doi.org/10.1016/j.lithos.2020.105756>
- Lehmann B, Ishihara S, Michel H, Miller J, Rapela C, Sanchez A, Tistl M, Winkelmann L (1990) The Bolivian tin province and regional tin distribution in the Central Andes: a reassessment. *Econ Geol* 85:1044–1058
- Lehmann B, Dietrich A, Heinhorst J, Métrich N, Mosbah M, Palacios C, Schneider HJ, Wallianos A, Webster J, Winkelmann L (2000) Boron in the Bolivian tin belt. *Miner Deposita* 35:223–232
- Lentz D, McAllister A (1990) The petrogenesis of tin- and sulfide mineralization at True Hill, southwestern New Brunswick. *Atlant Geol* 26:136–155
- Lerouge C, Gloaguen E, Wille G, Bailly L (2017) Distribution of In and other rare metals in cassiterite and associated minerals in Sn ± W ore deposits of the western Variscan Belt. *Eur J Mineral* 29:739–753
- Linnen RL, Pichavant M, Holtz F, Burgess S (1995) The effect of fO_2 on the solubility, diffusion, and speciation of tin in haplogranitic melt at 850°C and 2 kbar. *Geochim Cosmochim Acta* 59:1579–1588
- Longo AA, Dilles JH, Grunder AL, Duncan R (2010) Evolution of calc-alkaline volcanism and associated hydrothermal gold deposits at Yanacocha, Peru. *Econ Geol* 105:1191–1241
- Mao W, Zhong H, Yang J, Tang Y, Liu L, Fu Y, Zhang X, Sein K, Soe MA, Li J, Le Z (2020) Combined zircon, molybdenite, and cassiterite geochronology and cassiterite geochemistry of the Kuntabin tin-tungsten deposit in Myanmar. *Econ Geol* 115:603–625
- Marinov D (2011) Re-Os molybdenite geochronology from Michiquillay and Galeno porphyry copper deposits, Cajamarca, Perú. In: Barra F, Reich M, Campos E, Tornos F (eds) *Let's Talk Ore Deposits*, Proceedings of the 11th Biennial SGA Meeting, Antofagasta, Chile, Universidad Católica del Norte: Antofagasta, Chile pp 113–114
- McLaughlin DH (1924) *Geology and physiography of the Peruvian Cordillera*, Departments of Junin and Lima. *Geol Soc Am Bull* 35:591–632
- Mégard F (1984) The Andean orogenic period and its major structures in central and northern Perú. *J Geol Soc Lond* 141:893–900
- Mégard F, Caldas J, Paredes J, De la Cruz N (1996) *Geología de los cuadrángulos de Tarma, La Oroya y Yauyos*; Boletín 69; Instituto Geológico Minero y Metalúrgico del Perú: Lima, Peru, Mapas: 23-1, 24-1, 25-1. Scale 1(100):000
- Meng Y, Hu R, Huang X, Gao J (2017) Germanium in magnetite: a preliminary review. *Acta Geol Sin* 91:711–726
- Mišković A, Spikings RA, Chew DM, Košler J, Ulianov A, Schaltegger U (2009) Tectonomagmatic evolution of Western Amazonia: geochemical characterization and zircon U-Pb geochronologic constraints from the Peruvian Eastern Cordilleran granitoids. *Geol Soc Am Bull* 121:1298–1324
- Moore F, Howie RA (1979) Geochemistry of some Cornubian cassiterites. *Miner Deposita* 14:103–107
- Mrozek SA, Chang Z, Spandler C, Windle S, Raraz C, Paz A (2020) Classifying skarns and quantifying metasomatism at the Antamina deposit, Peru: insights from whole-rock geochemistry. *Econ Geol* 115:177–188
- Murciego A, Sanchez AG, Dusaouy Y, Pozas JM, Ruck R (1997) Geochemistry and EPR of cassiterites from the Iberian Hercynian Massif. *Mineral Mag* 61:357–365
- Nadoll P (2011) *Geochemistry of magnetite from hydrothermal ore deposits and host rocks – case studies from the Proterozoic Belt Supergroup, Cu-Mo-porphyry + skarn and Climax-Mo deposits in the western United States*. PhD thesis, The University of Auckland, New Zealand, 313 p
- Nadoll P, Angerer T, Mauk JL, French D, Walshe J (2014) The chemistry of hydrothermal magnetite: a review. *Ore Geol Rev* 61:1–32
- Nakamura Y, Shima H (1982) Fe and Zn partitioning between sphalerite and stannite. In: *Proceedings of the Joint Meeting of Society of Mining Geologists of Japan; The Japanese Association of Mineralogists, Petrologists and Economic Geologists and the Mineralogical Society of Japan*: Sendai, Japan (In Japanese), A-8
- Nambaje C, Eggins SM, Yaxley GM, Sajeev K (2020) Micro-characterization of cassiterite by geology, texture and zonation: a case study of the Karagwe Ankole Belt, Rwanda. *Ore Geol Rev* 124:103609
- Nascimento T, Souza V (2017) Mineralogy, stable isotopes ($\delta^{18}O$ and $\delta^{34}S$) and ^{40}Ar - ^{39}Ar geochronology studies on the hydrothermal carapace of the Igarapé Manteiga W-Sn Deposit, Rondônia. *Braz J Geol* 47:591–613
- Nassar NT, Graedel TE, Harper EM (2015) By-product metals are technologically essential but have problematic supply. *Sci Adv* 1:e1400180
- Neiva A (2008) Geochemistry of cassiterite and wolframite from tin and tungsten quartz veins in Portugal. *Ore Geol Rev* 33:221–238
- Noble DC, McKee EH (1999) The Miocene metallogenic belt of central and northern Peru. *Soc Econ Geol Spec Publ* 7:155–193
- Noble DC, Vidal CE, Perelló J, Rodríguez O (2004) Space-time relationships of some porphyry Cu-Au, epithermal Au, and other magmatic-related mineral deposits in Northern Peru. *Soc Econ Geol Spec Publ* 11:313–318
- Oen IS, Kager P, Kieft C (1980) Oscillatory zoning of a discontinuous solid-solution series: sphalerite-stannite. *Am Mineral* 65:1220–1232
- Parasyuk OV, Voronyuk SV, Gulay LD, Davidyuk GY, Halka VO (2003) Phase diagram of the CuInS-ZnS system and some physical properties of solid solutions phases. *J Alloy Compd* 348:57–64
- Patterson DJ, Ohmoto H, Solomon M (1981) Geologic setting and genesis of cassiterite-sulfide mineralization at Renison Bell, Western Tasmania. *Econ Geol* 76:393–438
- Patrick RAD, Dorling M, Polya DA (1993) TEM study of indium and copper-bearing growth-banded sphalerite. *Can Mineral* 31:105–117
- Pavlova GG, Palessky SV, Borisenko AS, Vladimirov AG, Seifert T, Phan LA (2015) Indium in cassiterite and ores of tin deposits. *Ore Geol Rev* 66:99–113
- Peralta E, Colquhoun W, El Rassi D, Johnston A, Searston S (2019) Technical report on the mineral resource estimate for the Ayawilca property, Department of Pasco, Peru, NI 43-101 Report. 329 p. https://www.tinkaresources.com/site/assets/files/5515/tinka_ayawilca_tr_final.pdf. Accessed 1 Jan 2021
- Pfiffner OA, Gonzalez L (2013) Mesozoic-Cenozoic evolution of the western margin of South America: case study of the Peruvian Andes. *Geosciences* 3:262–310
- Plimer IR, Lu J, Kleeman JD (1991) Trace and rare earth elements in cassiterite – sources of components for the tin deposits of the Mole Granite, Australia. *Miner Deposita* 26:267–274
- Pollard PJ, Pichavant M, Charoy B (1987) Contrasting evolution of fluorine- and boron-rich tin systems. *Miner Deposita* 22:315–321


- Pring A, Wade B, McFadden A, Lenehan CE, Cook NJ (2020) Coupled substitutions of minor and trace elements in co-existing sphalerite and wurtzite. *Minerals* 10:147
- Ramdohr P (1969) The ore minerals and their intergrowths, 1st edn. Elsevier, Amsterdam, p 1174
- Reich M, Román N, Barra F, Morata D (2020) Silver-rich chalcopyrite from the active Cerro Peabellón geothermal system, northern Chile. *Minerals* 10:113
- Ritterbush K, Rosas S, Corsetti F, Bottjer D, West J (2015) Andean sponges reveal long – term ecosystem shifts following the end – Triassic mass extinction. *Palaeogeog Palaeoclimat Palaeocol* 420:193–209
- Rodríguez R, Cueva E, Carlotto V (2011) Geología del cuadrángulo de Cerro de Pasco. INGEMMET, Carta Geológica Nacional (Boletín N° 144 Serie A, escala 1:50,000, 160 p)
- Rosas S, Fontboté L, Tankard A (2007) Tectonic evolution and paleogeography of the Mesozoic Pucará Basin, Central Peru. *J S Am Earth Sci* 24:1–24
- Rosenbaum G, Giles D, Saxon M, Betts PG, Weinberg RF, Duboz C (2005) Subduction of the Nazca Ridge and the Inca Plateau: insights into the formation of ore deposits in Peru. *Earth Planet Sci Lett* 239:18–32
- Rottier B, Kouzmanov K, Wälle M, Bendezú R, Fontboté L (2016) Sulfide replacement processes revealed by textural and LA-ICP-MS trace element analyses: example from the early mineralization stages at Cerro de Pasco, Peru. *Econ Geol* 111:1347–1367
- Rottier B, Kouzmanov K, Casanova V, Wälle M, Fontboté L (2018) Cyclic dilution of magmatic metal-rich hypersaline fluids by magmatic low-salinity fluid: a major process generating the giant epithermal polymetallic deposit of Cerro de Pasco, Peru. *Econ Geol* 113:825–856
- Rottier B, Kouzmanov K, Ovtcharova M, Ulianov A, Wälle M, Selby D, Fontboté L (2020) Multiple rejuvenation episodes of a silicic magma reservoir at the origin of the large diatreme-dome complex and porphyry-type mineralization events at Cerro de Pasco (Peru). *Lithos* 376–377:105766
- Rottier B, Kouzmanov K, Casanova V, Bouvier A, Baumgartner LP, Wälle M, Fontboté L (2021) Tracking fluid mixing in epithermal deposits – Insights from in-situ $\delta^{18}O$ and trace element composition of hydrothermal quartz from the giant Cerro de Pasco polymetallic deposit Peru. *Chemical Geology*. <https://doi.org/10.1016/j.chemgeo.2021.120277>
- Sack RO, Lynch JVG, Foit FF (2003) Fahlore as a petrogenetic indicator: Keno Hill Ag-Pb-Zn District, Yukon, Canada. *Mineral Mag* 67:1023–1038
- Sahlström F, Arribas A, Dirks P, Corral I, Chang Z (2017) Mineralogical distribution of germanium, gallium and indium at the Mt Carlton high-sulfidation epithermal deposit, NE Australia and comparison with similar deposits worldwide. *Minerals* 7:1–213
- Saintilan NJ, Sproson AD, Selby D, Rottier B, Casanova V, Creaser RA, Kouzmanov K, Fontboté L, Piecha M, Gereke M, Zambito IVJJ (2021) Osmium isotopic constraints on sulphide formation in the epithermal environment of magmatic-hydrothermal mineral deposits. *Chem Geol* 564:120053
- Scherrenberg AF, Jacay J, Holcombe RJ, Rosenbaum G (2012) Stratigraphic variations across the Marañón Fold-Thrust Belt, Peru: implications for the basin architecture of the West Peruvian Trough. *J S Am Earth Sci* 38:147–158
- Scherrenberg AF, Konh BP, Holcombe RJ, Rosenbaum G (2016) Thermotectonic history of the Marañón Fold-Thrust Belt, Peru: insights into mineralisation in an evolving orogeny. *Tectonophysics* 667:16–36
- Schorr S, Wagner G (2005) Structure and phase relations of the $Zn_{2x}(CuIn)_{1-x}S_2$ solid solution series. *J Alloy Compd* 396:202–207
- Schwarz-Schampera U, Herzig P (2002) Indium: geology, mineralogy, economics. Springer-Verlag, Berlin, p 257
- Scott SD, Barnes HL (1971) Sphalerite geothermometry and geobarometry. *Econ Geol* 66:653–669
- Sempere TPA, Acosta J (2019) Extension of the Late Triassic salt into western Peru: implications for Andean tectonics and mineral exploration. Proceedings of proEXPLO, Lima, 2019. <http://www.proexplo.com/2019/docs/programa/W03.pdf>. Accessed 1 February 2021
- Serranti S, Ferrini V, Umberto M, Cabri LJ (2002) Trace-element distribution in cassiterite and sulfides from Rubané and massive ores of the Corvo deposit, Portugal. *Can Mineral* 40:815–835
- Sillitoe RH (2004) Musings on future exploration targets and strategies in the Andes. *Soc Econ Geol Spec Publ* 11:1–14
- Sillitoe RH (2010) Porphyry copper systems. *Econ Geol* 105:3–41
- Sillitoe RH, Perelló J (2005) Andean copper province: tectonomagmatic settings, deposit types, metallogeny, exploration, and discovery. In: Hedenquist JW, Thompson JFH, Goldfarb RJ, Richards JR (eds) *Economic Geology 100th Anniversary Volume*. Society of Economic Geologists Inc., pp 845–890
- Smeds SA (1993) Herzenbergite (SnS) in Proterozoic granite pegmatites in north-central Sweden. *Mineral Mag* 57:489–494
- Spikings R, Reitsma MJ, Boekhout F, Mišković A, Ulianov A, Chiaradia M, Gerdes A, Schaltegger U (2016) Characterisation of Triassic rifting in Peru and implications for the early disassembly of western Pangaea. *Gondwana Res* 35:124–143
- Taylor RG (1979) *Geology of tin deposits*. Elsevier, The Netherlands, p 556
- Torres B, Melgarejo JC, Torró L, Camprubí A, Castillo-Oliver M, Artiaga D, Campeny M, Tauler E, Jiménez-Franco A, Alfonso P, Arce-Burgoa OR (2019) The Poopó polymetallic epithermal deposit, Bolivia: mineralogy, genetic constraints, and distribution of critical elements. *Minerals* 9:472
- Torró L, Melgarejo J, Gemmrich L, Mollinedo D, Cazorla M, Martínez Á, Pujol-Solà N, Farré-de-Pablo J, Camprubí A, Artiaga D, Torres B, Alfonso P, Arce O (2019a) Spatial and temporal controls on the distribution of indium in xenothermal vein deposits: the Huari District, Potosí, Bolivia. *Minerals* 9:304–340
- Torró L, Cazorla M, Melgarejo J, Camprubí A, Gemmrich L, Campeny M, Artiaga D, Torres B, Martínez Á, Tarrés M, Mollinedo D, Alfonso P, Arce O (2019b) Indium mineralization in the volcanic dome-hosted Ánimas–Chocaya–Siete Suyos polymetallic deposit, Potosí, Bolivia. *Minerals* 9:604–642
- Toulmin P, Barton PB (1964) A thermodynamic study of pyrite and pyrrhotite. *Geochim Cosmochim Acta* 28:641–671
- Vermeesch P (2018) IsoplotR: a free and open toolbox for geochronology. *Geosci Front* 9:1479–1493
- Wilson JJ (1963) Cretaceous stratigraphy of central Andes of Peru. *Am Assoc Pet Geol Bull* 47:1–34
- Wilson JJ, Reyes L (1964) Geología del cuadrángulo de Patatz: hoja 16-H. Serie a: Carta Geológica Nacional, Boletín 9:91p
- Wise M, Brown C (2011) Chemical composition of coexisting columbite-group minerals and cassiterite from the Black Mountain pegmatite, Maine. *Eur J Mineral* 23:817–828
- Wittmann A (1974) Indium. 49-A crystal chemistry. In: Wedepohl KH (ed) *Handbook of geochemistry*, Berlin, Springer-Verlag, vol. II/4, pp 49-A-1 - 49-A-8
- Xiang L, Romer RL, Glodny J, Trumbull RB, Wang R (2020) Li and B isotopic fractionation at the magmatic-hydrothermal transition of highly evolved granites. *Lithos* 376–377:105753
- Xu J, Cook NJ, Ciobanu CL, Li X, Kontonikas-Charos A, Gilbert S, Lv Y (2020) Indium distribution in sphalerite from sulfide–oxide–silicate skarn assemblages: a case study of the Dulong Zn–Sn–In deposit, Southwest China. *Miner Deposita* 56:307–324

- Zhang R, Lu J, Lehmann B, Li C, Li G, Zhang L, Guo J, Sun W (2017) Combined zircon and cassiterite U–Pb dating of the Piaotang granite-related tungsten–tin deposit, southern Jiangxi tungsten district, China. *Ore Geol Rev* 82:268–284
- Zhao Y, Chen S, Huang Y, Zhao J, Xiang T, Chen X (2019) U–Pb ages, O isotope compositions, Raman spectrum, and geochemistry of cassiterites from the Xi’ao copper–tin polymetallic deposit in Gejiu District. *Yunnan Province Minerals* 9:212
- Zoheir B, Lehmann B, Emam A, Radwan A, Zhang R, Bain WM, Steele-MacInnis M, Nolte N (2020) Extreme fractionation

and magmatic–hydrothermal transition in the formation of the Abu Dabbab rare-metal granite, Eastern Desert, Egypt, *Lithos* 352–353:105329

Publisher’s note Springer Nature remains neutral with regard to jurisdictional claims in published maps and institutional affiliations.

Authors and Affiliations

Diego Benites¹ · Lisard Torró¹  · Jean Vallance¹ · Oscar Laurent^{2,3} · Patrick Quispe¹ · Silvia Rosas¹ · María Francisca Uzieda⁴ · Christopher S. Holm-Denoma⁵ · Laura S. Pianowski⁵ · Antoni Camprubi⁶ · Vanessa Colás⁶ · Álvaro Fernández-Baca⁷ · Luis Giraldo⁷ · Cyril Chelle-Michou² · Jorge Sáez¹ · Kalin Kouzmanov⁴ · Lluís Fontboté⁴

✉ Lisard Torró
lisardtorro@hotmail.com

¹ Geological Engineering Program, Faculty of Sciences and Engineering, Pontifical Catholic University of Peru (PUCP), Av. Universitaria 1801, San Miguel, Lima 15088, Peru

² ETH Zürich, Department of Earth Sciences, Institute for Geochemistry and Petrology, Zürich, Switzerland

³ Present Address: CNRS, Géosciences Environnement Toulouse, Observatoire Midi-Pyrénées, 31400 Toulouse, France

⁴ Department of Earth Sciences, University of Geneva, CH-1205 Geneva, Switzerland

⁵ U.S. Geological Survey, Geology, Geophysics and Geochemistry Science Center, Denver, CO, USA

⁶ Instituto de Geología, Universidad Nacional Autónoma de México. Ciudad Universitaria, Coyoacán, CDMX 04510, México

⁷ Tinka Resources Limited, Av. Benavides 1579 Of. 306, Miraflores, Lima, Peru